

The photometric properties of a vast stellar substructure in the outskirts of M33

Alan W. McConnachie¹

alan.mcconnachie@nrc-cnrc.gc.ca

Annette M. N. Ferguson², Michael J. Irwin³, John Dubinski⁴, Lawrence M. Widrow⁵,

Aaron Dotter⁶, Rodrigo Ibata⁷, Geraint F. Lewis⁸

¹NRC Herzberg Institute of Astrophysics, 5071 West Saanich Road, Victoria, B.C., V9E

2E7, Canada ²Institute for Astronomy, University of Edinburgh, Royal Observatory,

Blackford Hill, Edinburgh EH9 3HJ, UK ³Institute of Astronomy, University of Cambridge,

Madingley Road, Cambridge CB3 0HA, UK. ⁴Department of Astronomy & Astrophysics,

University of Toronto, 50 St. George Street, Toronto, Ontario, Canada M5S 3H4

⁵Department of Physics, Engineering Physics, and Astronomy Queen's University,

Kingston, Ontario, Canada K7L 3N6 ⁶Department of Physics and Astronomy, University of

Victoria, 3800 Finnerty Road, Victoria, British Columbia, Canada V8P 5C2 ⁷Observatoire

de Strasbourg, 11, rue de l'Université, F-67000 Strasbourg, France ⁸Sydney Institute for

Astronomy, School of Physics, A29, University of Sydney, NSW 2006, Australia

Received _____; accepted _____

ApJ, in preparation

ABSTRACT

We have surveyed approximately 40 square degrees surrounding M33 with CFHT MegaCam/MegaPrime in the g and i filters out to a maximum projected radius from this galaxy of 50 kpc, as part of the *Pan-Andromeda Archaeological Survey* (*PAndAS*). Our observations are deep enough to resolve the top ~ 4 magnitudes of the red giant branch population in this galaxy. We have previously shown that the disk of M33 is surrounded by a large, irregular, low-surface brightness substructure. Here, we quantify the stellar populations and structure of this feature using the PAndAS data. We show that the stellar populations of this feature are consistent with an old population with $\langle [Fe/H] \rangle \sim -1.6$ dex and an interquartile range in metallicity of ~ 0.5 dex. We construct a surface brightness map of M33 that traces this feature to $\mu_V \simeq 33$ mags arcsec $^{-2}$. At these low surface brightness levels, the structure extends to projected radii of ~ 40 kpc from the center of M33 in both the north-west and south-east quadrants of the galaxy. Overall, the structure has an “S-shaped” appearance that broadly aligns with the orientation of the HI disk warp. We calculate a lower limit to the integrated luminosity of the structure of -12.7 ± 0.5 mags, comparable to a bright dwarf galaxy such as Fornax or Andromeda II and slightly less than 1% of the total luminosity of M33. Further, we show that there is tentative evidence for a distortion in the distribution of young stars near the edge of the HI disk that occurs at similar azimuth to the warp in HI. The data also hint at a low-level, extended stellar component at larger radius that may be a M33 halo component. We revisit studies of M33 and its stellar populations in light of these new results, and we discuss possible formation scenarios for the vast stellar structure. Our favored model is that of the tidal disruption of M33 in its orbit around M31.

Subject headings: galaxies: halos — galaxies: individual (M33, M31) — galaxies:
interactions — Local Group — galaxies: structure

1. Introduction

Rogstad et al. (1976) noted that they had succeeded in “turning three puzzles into one enigma” with their analysis of the Local Group spiral galaxy M33 (the Triangulum Galaxy). These authors postulated that a severe warp in its HI disk could explain simultaneously three phenomena observed in their 21cm dataset; the “wings” of that galaxy, its steep radial profile, and the “so-called weak component”. Subsequent radio observations have shown their postulate to be correct (Corbelli & Schneider 1997; Putman et al. 2009), but exactly why this galaxy formed a warp in the first place, and why no optical counterpart has been observed, have remained enigmatic since this pioneering study.

M33 ($1^h33^m51^s, 30^\circ39'36''$) is the third brightest spiral galaxy in the Local Group, with a luminosity of $M_V = -18.9$. It is a late-type spiral, Sc II-III, and shows no clear evidence of any bulge component (Bothun 1992; Minniti et al. 1993; McLean & Liu 1996). Its rotation curve indicates a total mass of $> 5 \times 10^{10} M_\odot$ within 16kpc (the radius of the last measured point; Corbelli & Salucci 2000), approximately one-tenth that of its giant neighbor, M31. There is considerable disagreement in the literature regarding the distance of M33, with estimates ranging from ~ 800 kpc to > 900 kpc (e.g., Galleti et al. 2004; Ciardullo et al. 2004; Tiede et al. 2004; McConnachie et al. 2004a, 2005; Brunthaler et al. 2005; Bonanos et al. 2006; Sarajedini et al. 2006; U et al. 2009 and references therein). However, given the distance of M31 ($D_{M31} = 785 \pm 25$ kpc; McConnachie et al. 2005) and the separation of M31 and M33 on the plane of the sky (~ 15 degrees), it is reasonable to consider M33 as the most luminous satellite of M31.

A deep survey of M33 with the 2.5 meter Isaac Newton Telescope Wide Field Camera (INT WFC), that resolves individual stars in this galaxy down to $V = 24.5$ and $i = 23.5$ (Vega mags) with $S/N \sim 5$, shows a relatively “pristine” galaxy, with no obvious distortions or substructures over the area surveyed (Ferguson et al. 2007). This is in stark contrast to

results for M31, where an identical survey over an initial survey area of ~ 25 square degrees (Ferguson et al. 2002; later extended to ~ 40 square degrees; Irwin et al. 2005) revealed copious substructures. The most prominent of these was a giant stellar stream (Ibata et al. 2001) that reached to the edge of the survey area, as well as various other streams, overdensities and new dwarf galaxies (e.g., Zucker et al. 2004a,b; McConnachie et al. 2003, 2004b; Irwin et al. 2008). That M33 does not display the same richness of structures as M31 may in whole or in part be due to its significantly lower mass (e.g., Purcell et al. 2007).

A subsequent survey of M31 and M33 by Ibata et al. (2007), using the 1 degree field-of-view MegaCam/MegaPrime camera on the 3.6 meter Canada-France-Hawaii telescope (CFHT), identified stars to the deeper magnitude limits of $g \simeq 25.5$, $i \simeq 24.5$ (AB mags) at a $S/N = 10$. They contiguously map the entire south-east quadrant of M31 to a radius of 10 degrees (~ 150 kpc), and extend the survey area along the southern minor axis of M31 to connect with M33. They trace the radial surface brightness profile of M31 as it declines in the south-east quadrant to large radius, at which point the profile starts to increase again (see their Figure 38). Ibata et al. (2007) attribute this rise to a direct detection of the M33 stellar halo.

Building upon these previous surveys, the *Pan-Andromeda Archaeological Survey* (PAndAS; McConnachie et al. 2009), a Large Program on the CFHT, is contiguously mapping the entire halo of M31 out to a maximum projected radius of 150 kpc, and the surroundings of M33 out to a maximum projected radius of 50 kpc. One of the most striking discoveries presented in McConnachie et al. (2009) from the first year of the survey is the presence of a very large, low surface brightness, stellar substructure surrounding M33, and which extends out to several times the radius of the classical disk of M33. In this contribution, we examine in more detail the properties of this vast structure, as observed with the CFHT/MegaPrime data.

The format of this paper is as follows. In Section 2, we summarize the design on the PAndAS survey and overview the data as it relates to this study. In Section 3, we analyze and quantify the structure and stellar populations of the M33 substructure. In Section 4, we discuss our results in the context of the evolutionary history of M33 and previous studies of its disk and halo populations. Section 5 summarizes. Throughout this paper, we adopt a distance modulus for M33 of $(m - M)_0 = 24.54 \pm 0.06$ (809 ± 24 kpc; McConnachie et al. 2004a, 2005).

2. Preliminaries

2.1. Survey strategy

PAndAS is a Large Program on the 3.6 meter Canada-France Hawaii Telescope which uses the 0.96×0.94 degree field of view MegaPrime wide field camera to obtain g, i imaging of M31, M33 and their environs. This instrument consists of a mosaic of 36 2048×4612 pixel CCDs with a pixel scale of 0.187 arcsec/pixels $^{-1}$ at the center of the detector. Data acquisition for PAndAS started in the 2008B observing semester (S08B) and will continue until S10B, with the aim of contiguously imaging M31 and M33 out to projected radii of ~ 150 kpc and ~ 50 kpc, respectively, representing a total area of > 300 square degrees. This survey builds upon earlier CFHT/MegaPrime imaging of M31 and M33 from PI programs by R. Ibata (Martin et al. 2006; Ibata et al. 2007) and A. McConnachie (McConnachie et al. 2008). First results from PAndAS, showing the full extant survey area as at the end of S08B, are given in McConnachie et al. (2009).

Figure 1 shows the location of 40 MegaPrime fields centered on M33 in a tangent plane projection, where open squares represent CFHT/MegaPrime observations taken in S08B, and hatched fields show earlier fields presented in Ibata et al. (2007). The solid angle

subtended by these fields is equivalent to $\sim 7800 \text{ kpc}^2$ at the distance of M33. The inner ellipse represents the “edge” of the optical disk of M33 (70.8×41.7 arcmins diameter¹, the radius at which the disk surface brightness reaches $\mu_B \simeq 25 \text{ mags arcsec}^{-2}$). The major and minor axes are shown, and the dashed outer circle corresponding to a maximum projected radius of 50 kpc at the adopted distance of M33.

We adopt a similar observational strategy to the earlier PI programs, whereby we expose for 1350 seconds in g and i , split into 3 dithered sub-exposures of 450 seconds. All of our observations were taken in generally excellent seeing conditions, with a median $FWHM$ in the new data of better than 0.65 arcsecs. This is generally sufficient to reach $g \simeq 25.5$ and $i \simeq 24.5$ (AB mags) with $S/N = 10$. In some cases, more than three exposures were taken (at the discretion of CFHT staff to ensure the requested observing conditions were met), and in these cases the viable images were included in the stacking procedure, weighted according to noise/seeing.

2.2. Data processing and calibration

The CFHT/MegaPrime data were pre-processed by CFHT staff using the *Elixir* pipeline, which accomplishes the usual bias, flat, and fringe corrections and also determines the photometric zero point of the observations. These images were then processed using a version of the CASU photometry pipeline (Irwin & Lewis 2001) adapted for CFHT/MegaPrime observations. The pipeline includes re-registration, stacking, catalogue generation and object morphological classification, and creates band-merged g, i products for use in the subsequent analysis. The CFHT g and i magnitudes are de-reddened on a source-by-source basis using the Schlegel et al. (1998) IRAS maps, such that

¹Values taken from the NASA Extragalactic Database

$g_0 = g - 3.793E(B - V)$ and $i_0 = i - 2.086E(B - V)$, where g_0 and i_0 are the de-reddened magnitudes. Regnault et al. (2009) discuss many issues relating to the calibration of CFHT/MegaPrime photometry, and the data presented here are accurate at the level of $\pm 5\%$ peak-to-peak (judging from overlap regions between fields). This is sufficiently accurate for the present analysis, and a future contribution will discuss in more detail the calibration of the dataset.

The i -band photometry of the hatched fields in Figure 1 (observed in S05B) was taken with a different filter than the other fields (observed in S08B) due to the filter being replaced by CFHT in 2007. The correction between the two generations of photometry is expected to be small, and we derive it by searching for common objects in areas of overlap between the earlier imaging and the new data. To ensure a high quality fit, we use only those objects robustly identified as stellar in all 4 filters (the old and new i filter, and the two generations of g -band data), which do not lie near the edges of CCDs, and which have photometric errors less than 0.1 mags in all filters. Figure 2 shows the difference in the i -band photometry as a function of color (where i_1 refers to the new i -filter and i_2 refers to the old i -filter). The two filters have similar throughput at a color of $(g - i) \simeq 1.6$ and there is a slight gradient over the color range of interest (~ 0.07 mags between $(g - i_2) = 0.5$ and $(g - i_2) = 2.0$). The red points and error bars show the binned data (50 points per bin) and the blue line shows the best linear fit to the data, described by

$$i_2 - i_1 = -0.045(g - i_2) + 0.073 . \quad (1)$$

We use Equation 1 to transform all i -band photometry taken with the previous i -filter onto the same scale as the new i -band data.

Our final photometric uncertainties as a function of magnitude are shown in Figure 3 for each filter. Data for the central field, where crowding is very significant, is not shown.

The distinct sequences in Figure 3 are due to fields taken in different observing conditions. Generally, the mean uncertainty is smaller than 0.2 mags for $g \leq 25.5$ and $i \leq 24.5$.

2.3. Stellar isochrones

Figure 4 shows a comparison between the throughput of the CFHT and SDSS filter systems. While the systems are fairly similar in r , in the g and i filters there are some differences. In particular, the CFHT g filter is shifted to the red in comparison to the SDSS equivalent, and the CFHT i filter is broader than the SDSS equivalent by $\sim 250\text{\AA}$ towards the red end of the spectrum. Since we have well-determined atmospheric transmissions for Mauna Kea and for the overall throughput of CFHT, and that these are different to their SDSS counterparts, we decided to construct isochrones in the CFHT photometric system. To achieve this, isochrones from the Dartmouth Stellar Evolution Database (Dotter et al. 2007, 2008) were transformed to the CFHT system using filter response functions for the five broadband filters, combined with the throughput of the telescope optics, the quantum efficiency of the MegaPrime CCD, and the atmospheric transmission at Mauna Kea². The magnitudes were normalized to Vega using the flux-calibrated spectrum provided by Bohlin (2007) and then adjusted to the CFHT AB magnitude system by applying the appropriate offsets³. Bolometric corrections were then obtained using the grids of synthetic spectra described in Section 4 of Dotter et al. (2008). A grid of isochrones was created for $-2.5 \leq [\text{Fe}/\text{H}] \leq 0$ dex at $[\alpha/\text{Fe}] = 0, +0.2$, and $+0.4$ dex and $[\text{Fe}/\text{H}] = +0.3$ and $+0.5$ dex at $[\alpha/\text{Fe}] = 0$ and $+0.2$ dex.

Figure 5 shows a comparison between the CFHT isochrones (dashed lines) and globular

²<http://www.cfht.hawaii.edu/Instruments/Imaging/MegaPrime/specsinformation.html>.

³<http://www.cfht.hawaii.edu/Instruments/Imaging/MegaPrime/specsinformation.html>

cluster fiducial sequences for M92, M3 and M71 (solid lines, left to right) from Clem et al. (2008). The assumed apparent distance moduli in g and adopted $E(B-V)$ are (14.64, 0.04), (15.05, 0.03) and (13.79, 0.26) for M92, M3 and M71, respectively. For each cluster, we compare to 14Gyr isochrones with appropriate $[Fe/H]$ and $[\alpha/Fe]$ values, as given in the key in Figure 5. Over the displayed magnitude range, the isochrones provide excellent matches to the globular cluster sequences, implying that these isochrones are a good reference system for which to compare to real stellar populations. We note, however, that for this particular study we are concerned only with the RGB phase of stellar evolution. For reference, at $[Fe/H] = -1.5$ dex for a 12Gyr population, the isochrones shift redward by 0.05 mags in going from $[\alpha/Fe] = 0$ to $[\alpha/Fe] = +0.2$. Note that the Dartmouth isochrone set used here are generally redder at a given metallicity on the RGB than the Padova isochrones (Girardi et al. 2004) used by Ibata et al. (2007), leading to maximum difference in RGB metallicity for individual stars of a few tenths of a dex (see the comparison in Dotter et al. 2007).

3. Photometric analysis of the substructure surrounding M33

3.1. Global color-magnitude diagrams

Figure 6 shows the overall g_o and i_o color-magnitude diagrams (CMDs; left and right panels, respectively) for all stellar sources in the M33 survey area (excluding the central field). Only stars robustly identified as stellar in both filters are shown, corresponding to $> 650\,000$ stars. The CMDs are plotted as Hess images with 0.025×0.025 mag pixels and displayed with logarithmic scaling. Overlaid on each CMD are isochrones for a 12 Gyr, $[\alpha/Fe] = 0.0$, stellar population shifted to the distance modulus of M33, with $[Fe/H] = -2.5, -2, -1.5, -1$ and -0.5 dex.

Several features are obvious in Figure 6, not all of which represent components of M33 and its surroundings. The near-vertical sequences in both CMDs at $(g - i)_o \simeq 0.1$ are the main-sequence turn-off (MSTO) populations in the Galactic halo along our line of sight to M33. Two distinct main sequence features are visible in each CMD, indicating the presence of considerable (sub)structure in this region of the Milky Way halo (e.g., see Rocha-Pinto et al. 2004; Martin et al. 2007). In addition to the Galactic halo, a contribution from the Galactic disk is also visible in Figure 6: the majority of stars redder than $(g - i)_o > 2$ at all magnitudes represent the locus of foreground dwarfs in the disk of the Milky Way, and the density distribution of this population increases to the north of the survey. Finally, compact galaxies at typical redshifts of $z \sim 0.5$ that are misidentified as stars become a significant source of contamination at faint magnitudes ($g_0, i_0 > 24$), and tend to have predominantly bluer colors.

The stellar isochrones in Figure 6 show the locus of the CMD that contains red giant branch (RGB) stars in M33. Approximately 200 000 stellar objects are bounded by these isochrones (excluding the central field). At faint magnitudes, contamination of this locus increases due to the galaxies misidentified as stars; at redder colors (typically more metal-rich RGB stars at a given age, or older RGB stars at a given metallicity) contamination of this locus increases due to the foreground Galactic disk stars. If present, asymptotic giant branch (AGB) stars, typically representative of an intermediate-age stellar population, may occupy a similar locus to the RGB, and can extend to magnitudes significantly brighter than the tip of the RGB (e.g., Table 7 of Rejkuba et al. 2006). Young main sequence and blue-loop stars are also visible in Figure 6 as bright sources with $(g - i)_o < 0$.

3.2. Stellar population maps

3.2.1. Contaminants

Prior to examining the spatial distribution of the stellar populations in M33, it is important to understand the distribution of sources that could act as contamination and influence our results. To this end, Figure 7 shows tangent plane projections of the density distribution of the various types of sources that can act as contamination in our study of the M33 stellar populations. These maps use a pixel size of 1.2×1.2 arcmins, are unsmoothed and are displayed with linear scaling. The left panel shows stellar sources in the Galactic halo, here traced by stars within the color-magnitude cut $19.0 < i_0 < 22.0$, $0.1 < (g - i)_0 < 0.6$ (halo turnoff stars). In the central parts of M33, this color cut picks up some blue loop stars in the disk of the galaxy. The central panel shows stellar sources in the Galactic disk, here traced by stars within the color-magnitude cut $17.0 < i_0 < 20.0$, $1.5 < (g - i)_0 < 3.0$ (red disk dwarfs). In the central parts of M33, this color cut picks up some bright AGB and red supergiant stars in the disk of the galaxy. The right panel shows extended sources (galaxies) identified by our star-galaxy classification algorithm, within the luminosity range $17.0 < i_0 < 23.5$. Any faint, compact, galaxies that have erroneously been classified as stars are expected to have a broadly similar distribution to the overall galaxy population (extended sources). In the main body of M33, the high degree of crowding causes some blended stellar sources to be classified as extended sources; in the very central regions of M33, crowding prevents sources being identified at fainter magnitudes, creating an apparent hole in the distribution.

The Galactic halo and disk stars are relatively smoothly distributed in Figure 7, insofar as there are no obvious large scale substructures. The Galactic disk is located towards the north of the survey but the gradient is not so extreme that it shows up with the linear scaling of Figure 7 (M33 has Galactic coordinates $l = 133.6^\circ$, $b = -31.3^\circ$). The galaxy

distribution is distinct to the stars, and shows clear evidence of clustering.

3.2.2. *The red giant branch population*

Figure 8 shows a tangent plane projection of the density distribution of all candidate RGB stars with $i_0 \leq 23.5$. This limit has been chosen to ensure a very high completeness level in the data and small photometric uncertainties. These stars lie in the color-magnitude locus bounded by 12 Gyr, $[\alpha/Fe] = 0.0$, isochrones, with metallicities between $-2.5 \leq [Fe/H] \leq -0.2$ dex, shifted to the distance modulus of M33. This map was created with 1.2×1.2 arcmins pixels, then repeatedly smoothed 3 times using a linear filter with a width of 5 pixels, and displayed with logarithmic scaling.

In Figure 8, the concentration at $(\xi, \eta) \approx (-2.1^\circ, 2.6^\circ)$ is due to the globular cluster system of the background elliptical galaxy NGC 507. Due to the excellent seeing of the observations, these background globular clusters appear as individual point sources with colors similar to blue RGB stars. The slight north-to-south gradient visible over the image is due to contamination from the Galactic disk in the redder part of the RGB. The newly discovered M31/M33 satellite, Andromeda XXII (Martin et al. 2009), is barely visible in this plot at $(\xi, \eta) \approx (-1.4^\circ, -2.6^\circ)$. The disk of M33 is visible, and clearly extends further than the radius marked by $\mu_B \simeq 25$ mags arcsec $^{-2}$.

Of particular interest to this contribution is the low-level, irregular distribution of RGB stars surrounding the disk of M33, discovered by McConnachie et al. (2009). Extensions stretching toward the north-west and south-east, broadly aligned with the direction to M31, are visible in Figure 8; the component in the north-west appears to reach a maximum projected radius from M33 of ~ 3 degrees (42 kpc), 3 times further out than the main disk of the galaxy. In the south-east, the extension appears to reach to a projected radius of

roughly 2 degrees (28 kpc).

3.3. Color-magnitude diagrams and photometric metallicity

Red outlines in Figure 8 show regions selected to probe the stellar populations in the outer regions of M33. The red elliptical annulus and the rectangular areas labeled H1, H2, S1, S2 and S3 probe the outer part of the M33 disk, two putative halo fields, two fields on the north-western extent of the substructure and one field on the southern substructure, respectively. Each of these has an area of 0.35 square degrees. H1 and H2 are placed at similar distances from M33 as the substructure fields and probably contain broadly similar numbers of halo stars. The disk annulus has a mean semi-major axis of $a = 49.6$ arcmins (11.7 kpc) and a width on the major axis of 7.1 arcmins (1.7 kpc). The larger rectangular areas, labeled A and B, are one degree wide strips in Galactic latitude (centered at $l = 135.7^\circ$ and $l = 130.9^\circ$, respectively), that probe large areas of the survey on the east and west side of M33, and which will be used to explore the variation of foreground stellar populations with Galactic latitude.

Figure 9 shows the CMDs for the disk annulus field, H1, H2 (top row, left to right, respectively), S1, S2 and S3 (middle row, left to right, respectively), and areas A and B (bottom row, left and right, respectively). Isochrones corresponding to $[\text{Fe}/\text{H}] = -0.5, -1.0, -1.5, -2.0, -2.5$ dex are overlaid on area B for reference. The disk field appears to have the largest mix of stellar populations; in addition to the foreground populations, a broad RGB is visible, indicating a significant range in age and/or metallicity. A population of blue, $(g-i)_o < 0$, stars is also visible, and a luminous AGB population may also be present but is difficult to discern from the bright RGB and Galactic disk foreground population. This field stands in contrast to the two putative halo fields. In both H1 and H2, the only stellar populations that are present in any significant number are the foreground

populations and faint, bluish ‘stars’ that could all be misidentified galaxies. However, H2 in particular shows some evidence of a very weak RGB. Thus a low level halo population in M33 cannot be ruled out, and may vary spatially. This will be investigated in more detail in a future contribution; here our focus is towards the large stellar substructure.

In Figure 9, it is striking that the CMDs of S1, S2 and S3 are all similar, and distinct to the disk annulus and putative halo fields. In particular, the similarity of the S3 field with S1 and S2, despite being located on the opposite side of the M33 disk, is strongly suggestive of a connection between the substructure in the south-east and that in the north-west. The RGB population in each of these field is narrower than found in the disk annulus, and seems to lack the population of redder RGB stars that are found in the disk field.

Figure 10 further quantifies the morphology of the RGB populations. The upper panel shows photometric metallicity distribution functions (MDFs) for the combined halo fields (H1 and H2; dot-dashed histogram), disk annulus field (dashed histogram), and the combined substructure fields (S1, S2 and S3; solid histogram). The histograms are scaled to have the same area. The distribution functions have been created by comparing each star with $i_0 \leq 23.5$ to 12Gyr, $[\alpha/Fe] = 0$, isochrones, in the range $-2.5 \leq [Fe/H] \leq -0.2$ dex, shifted to the distance modulus of M33. A bilinear interpolation is conducted in color-magnitude space to find the metallicity of the isochrone that best matches with the star’s position. These MDFs are uncorrected for foreground contamination, which is clearly a significant contributor at higher ($[Fe/H] \gtrsim -0.7$ dex) metallicity. It is for this reason that we do not include isochrones more metal-rich than $[Fe/H] = -0.2$ dex, since here contamination from MW disk dwarfs is severe and, as Figure 10 demonstrates, few M33 RGB stars are this metal-rich anyway.

Error bars in the top panel of Figure 10 quantify the robustness of the MDFs to photometric errors. The position of each star in the CMD is modelled as a two dimensional

Gaussian, centered at the colour and magnitude of the star and with widths equal to the photometric uncertainties. We calculate the MDF for each component a total of 1000 times, where in each realisation we select the colour and magnitude of each star from its distribution and conduct the interpolation as standard. The error bars show the standard deviation in each bin over the 1000 realisations.

The lower panel of Figure 10 shows the foreground corrected MDFs for the disk annulus field and the combined substructure field (dashed and solid histograms, respectively). Here, the putative halo MDF has been subtracted, scaled in order to match the number of bright stars ($i \leq 21$ mags) in the disk/substructure field. Since bright stars are mostly foreground stars, then this scaling accounts for possible variation in the foreground level across the survey region. To first order, any weak M33 halo signature in the disk and substructure fields will also have been removed. Note that the larger fields, A and B, could also be used for subtraction here, but these are unlikely to contain many M33 halo stars given their larger distances from the galaxy.

With the usual caveats regarding the age and homogeneity of the stellar populations, Figure 10 implies that the mean (median) metallicity of the M33 substructure is $[Fe/H] \simeq -1.55$ dex (-1.6 dex), and is indicated in Figure 10 by the dotted (dot-dashed) line. The interquartile range for the distribution is $IQR = 0.5$ dex, which will include a slight broadening due to photometric uncertainties that is small in comparison to systematic uncertainties. While the disk annulus has stars that are as metal-poor as those found in the substructure, and has a similar IQR (0.6 dex) its mean (median) metallicity is notably higher, with $[Fe/H] \simeq -1.25$ dex (-1.2 dex). Also, while the peak metallicity of the substructure is close to its mean value, the peak metallicity of the disk is higher still, at $[Fe/H] \sim -0.95$ dex. Note that adopting a 9 Gyr age assumption would act to increase our metallicity estimates by ~ 0.2 dex.

Finally, Figure 11 shows the background-corrected Hess diagrams corresponding to the MDFs shown in the lower panel of Figure 10. Here, the Hess diagram corresponding to the combined “halo” fields has been subtracted from the disk and combined substructure CMDs, using the same scaling as for the MDFs. The pixels used in Figure 11 are 0.05×0.05 mags, and for clarity only positive residuals are shown on a linear scale. A 12Gyr, $[\alpha/Fe] = 0.0$, $[Fe/H] = -1.2$ dex isochrones (the mean metallicity of the disk field) is overlaid in both panels for reference. Figure 11 also shows that the stars in both the disk and substructure regions extend to equivalently blue (metal-poor?) colours, and that the main difference between the populations is at the red (metal-rich?) end.

3.4. Surface brightness distribution of M33 substructure

We now investigate in more detail the surface brightness distribution of the M33 substructure. The previous MDF analysis suggests that, while RGB stars of all photometric metallicities are present in the structure, the majority have $-2.0 \leq [Fe/H] \leq -1.0$ dex (Figure 10). We therefore adopt this cut to enhance the substructure relative to other features in our survey, and we continue to use the $i_0 \leq 23.5$ magnitude cut.

3.4.1. Background variations

Figure 12 investigates how the Galactic foreground varies as a function of Galactic latitude for stars that coincide with our “optimal” RGB metallicity cut of $-2.0 \leq [Fe/H] \leq -1.0$ dex and $i_0 \leq 23.5$. Here, we have plotted the density variation with Galactic latitude of stars that satisfy this cut and which are located in the 1 degree wide strips highlighted in Figure 8 as “A” and “B”, centered at $l = 135.7^\circ$ and $l = 130.9^\circ$, respectively. These strips were purposely positioned away from the substructure on either

side of our survey to probe large-scale variations in the foreground. Circular points in Figure 12 correspond to the density distribution in strip A and triangles correspond to strip B.

Figure 12 shows that the variation in the foreground over our survey area in our optimal RGB metallicity cut is relatively stable. In particular, there are no significant trends with Galactic latitude - the density of counts do not vary systematically between $b = -29^\circ$ and $b = -33^\circ$. In addition, the counts in strip A and strip B, separated by nearly 5° in Galactic longitude, are approximately the same; dotted lines in Figure 12 indicate the mean and 1σ variations in density for strip A, and dashed lines indicate the same for strip B. There is little difference between the means, and they lie within the 1σ variation. As such, we conclude that a constant background is a suitable approximation for the subsequent surface brightness analysis.

3.4.2. *Stellar density - surface brightness*

Figure 13 is the stellar density map for our chosen optimal RGB metallicity cut ($-2.0 \leq [Fe/H] \leq -1.0$ dex and $i_o \leq 23.5$), constructed in an identical way to Figure 8, and shown with linear scaling. The grey contour level shows the 1σ detection threshold in star counts and the black contours show $2, 5, 8$ and 12σ detection thresholds. The substructure is seen clearly in this image, and extends out nearly as far as the 50 kpc boundary of the survey (shown with a dashed line). These low level contours also suggest that the southern extension of the substructure may extend out as far as its northern counterpart, although at large radius it is a lower surface brightness, less coherent, feature than in the north.

Figure 14 shows background-corrected radial profiles for M33, constructed in 1 degree wide strips, in two orthogonal directions, using identical cuts as for Figure 13. The top

panel shows the radial profile in an “on-stream” region, and the bottom panel shows the profile in an “off-stream” region. Each bin is chosen so that the signal-to-noise due to Poisson errors in that bin (prior to background subtraction) is at least 10, and the displayed error bars additionally include the uncertainty in the background. Here, θ refers to the angle, measured east-from-north, from the northern semi-major axis of M33. Dashed lines correspond to the radius of the $\mu_B = 25 \text{ mag arcsec}^{-2}$ isophote. The substructure is clearly visible in the top panel of Figure 14 as an extended, slowly-declining, component. A north-south asymmetry is present, with the northern component more dominant out to larger radius than in the south. This feature is also present in the “off-stream” region, particularly in the east, but does not extend as far as in the “on-stream” regions. Beyond $1 - 1.5$ degrees in the “off-stream” region, there are hints of a slowly-declining component. Presumably this can be attributed to an extended halo in M33, also hinted at in the “halo” CMDs in Figure 9. However, other interpretations may exist, and we will return to this topic in a later paper.

Figures 13 and 14 show density distributions of a subset of candidate RGB stars; to convert this into surface brightness necessarily requires some assumption about the luminosity function to correct for the unresolved stellar component. In Section 3.3, we showed that the resolved populations in the substructure are consistent with a relatively metal-poor ($[Fe/H] \simeq -1.5 \text{ dex}$) population, similar to that of some of the dwarf spheroidal (dSph) galaxies around M31 (e.g., Da Costa et al. 1996, 2002; McConnachie et al. 2005). The two brightest dSph galaxies that completely lie within the first-year PAndAS footprint are Andromeda I and III, and these have independent measurements of their total luminosity based on unresolved light (McConnachie & Irwin 2006). As such, these dSphs can provide us with an observationally-motivated transformation between RGB star counts and integrated luminosity. Implicit in this technique is that the luminosity function of the substructure is the same as for Andromeda I (III).

Our adopted distance modulus for M33 of $(m - M)_o = 24.54 \pm 0.06$ corresponds to a magnitude at the tip of the RGB of $I_o = 20.49$ (McConnachie et al. 2005). In the CFHT filter system, this corresponds to $i_o = 20.97$ (see the transformations given in Ibata et al. 2007) for a mean color at the tip of the RGB of $(V - I) \simeq 1.7$ (e.g., McConnachie et al. 2004a). Thus Figure 13 shows stars within the top 2.5 magnitudes of the RGB population in M33, given our cut-off magnitude of $i_o = 23.5$.

McConnachie & Irwin (2006) measure integrated luminosities of $M_V^I = -11.8 \pm 0.1$ and $M_V^{III} = -10.2 \pm 0.3$ for Andromeda I and III, respectively. Using these galaxies’ half-light radii, ellipticity and position angles, as measured by the same authors, we record the total luminosity of stars observed in the PAndAS data within 2.5 mags of the tip of the RGB and within one half-light radius from each of these galaxies. We correct this value for foreground by comparison to nearby regions, and we multiply the final value by two to obtain the total “RGB luminosity” of Andromeda I and III. We require a 2.30 and 2.18 magnitude offset for Andromeda I and III, respectively, to correct the RGB luminosity to the total integrated luminosity. This implies that the top 2.5 magnitudes of the RGB are contributing $\sim 10 - 15\%$ of the total light of these galaxies, which seems reasonable for an old population (e.g., Figure 2 in Renzini & Fusi Pecci 1988).

To convert Figure 13 to a background-corrected surface brightness scale, we measure the total luminosity of all the stars in each pixel of the unsmoothed version of Figure 13, and subtract the background. We correct this luminosity for RGB stars that are not included in our metallicity cut (Figure 10 shows that 69% of RGB stars with $i_o \leq 23.5$ are included in our optimal metallicity cut, $-2.0 \leq [Fe/H] \leq -1.0$ dex). We then smooth the map as before, and correct the value of each pixel by 2.30 (2.18) magnitudes using the conversion for Andromeda I (III).

Figure 15 plots the relation between the number of RGB stars in each pixel of Figure 13

and the integrated luminosity of the pixel as derived above (using the Andromeda I transformation). Arrows on the x -axis show the 1, 2, 5, 8 and 12σ number density contour levels from Figure 13. We fit a simple linear relationship to the data points in Figure 15 by binning the data above $n_{RGB} = 500 \text{ stars degree}^{-2}$ and use this relationship to calculate the surface brightness values corresponding to our contour levels. These are listed in full in Table 1, for both the Andromeda I and III transformations. The right vertical axis of Figure 15 shows the surface brightness scale for the Andromeda I transformation. Note that, at low stellar density, this relationship overestimates the actual “observed” luminosity density, since star counts and luminosity are only in direct proportion if the luminosity function is well sampled. At low star count levels, more luminous stars, that are intrinsically more rare than less luminous stars, are undersampled. Thus regions with low star counts are found to be underluminous compared to expectations from regions with higher star counts. To illustrate this, we fit a second linear relationship to Figure 15 using only regions with $n_{RGB} \leq 350 \text{ stars degree}^{-2}$. The surface brightness scale that this produces is listed in Table 1 in parentheses.

The background-subtracted surface brightness levels listed in Table 1 clearly have large systematic uncertainties. These include the unknown form of the true luminosity function; the uncertainty in the integrated luminosity of the system we are normalizing to (Andromeda I and III); the stochastic variations in stellar density/stellar luminosity in sparse regions. The spread in surface brightness values in each row of Table 1, combined with the uncertainties in total luminosities of Andromeda I and III, suggests that the zero-point of the surface brightness scale is accurate to the level of $\pm 0.5 \text{ mags arcsec}^{-2}$.

3.4.3. Integrated light

We integrate the surface brightness map to calculate the total luminosity of the substructure surrounding M33. Defining the edges of the substructure by the 2σ and 12σ contours in Figure 13 results in a total luminosity of $M_V = -12.7 \pm 0.5$ after correction to the distance modulus of M33. This number is a lower limit since it assumes there is a hole in the middle of the substructure delineated by the 12σ contour. If instead we allow for an additional constant contribution to the flux from within this area equal to $30.8 \text{ mag arcsec}^{-2}$ (see Table 1), then the luminosity of the substructure increases by ~ 0.4 mags. Thus the total luminosity of this feature is of order $\sim 1\%$ of the total luminosity of M33. For comparison, the Fornax dwarf galaxy - one of the brightest dwarf spheroidal galaxies in the Local Group - has a luminosity of $M_V = -13.2$ (Mateo 1998).

3.5. Distribution of young stars

The top panel of Figure 16 shows a tangent plane projection of the position of all blue stars with $(g - i)_o < 0$ and $i_o < 23.5$ mags, that predominantly selects bright main sequence and blue-loop stars, indicative of a young population. Foreground contamination in this color interval is minimal. An annulus sampling stars in the outer disk is shown, where the inner edge corresponds to the radius at which $\mu_B = 25 \text{ mags arcsec}^{-2}$, and the outer edge is 1.25 times further out. Circular points in the lower panel of Figure 16 show the variation in stellar density around this annulus as a function of θ , defined earlier. Error bars show the Poisson uncertainties. Two clear overdensities are visible, at $\theta \simeq 130^\circ$ and $\theta \simeq 310^\circ$. It is notable that these overdensities of young stars are separated by 180° , and that they have a similar orientation to the RGB overdensity and the HI warp. Thus it is not just the gas and *evolved* stars in M33 that have a distorted distribution, and it is perhaps not surprising that the young stars appear to follow the same distorted distribution as the underlying gas.

4. Discussion

4.1. Revisiting detections of the M33 stellar halo

Ibata et al. (2007) measure the radial surface brightness of M31 in the direction of M33. The M31 surface brightness is shown to decrease to $\sim 33 \text{ mags arcsec}^{-2}$ at $\sim 11^\circ$ ($\sim 165 \text{ kpc}$) from M31 before it starts increasing again approaching M33. This is attributed to a detection of M33’s stellar halo. However, with the completion of azimuthal coverage around M33 presented herein, it is clear that Ibata et al. (2007) had in fact detected the north-eastern extension of the stellar structure examined here, and not an extended, bona-fide, halo population.

McConnachie et al. (2006) analyze Keck/DEIMOS spectroscopy of giant stars in two fields on the southern minor axis of M33, 38 arcmins (9 kpc) from the center of the galaxy. The dominant component visible in the kinematics for this field is the disk. In addition, they also identify a population of stars at more negative velocities than the systemic velocity of M33 ($v_h = -179 \text{ km s}^{-1}$). These stars are consistent with belonging to a pressure supported stellar halo, with a dispersion of $\sigma \sim 50 \text{ km s}^{-1}$. However, in light of the stellar substructure identified in the PAndAS data, the analysis by McConnachie et al. (2006) needs to be revisited. Their interpretation of the M33 stellar kinematics was made with reference to a simple model of a regular, unperturbed, stellar disk with a rotation curve similar to that observed in the HI (Corbelli 2003). Using a more complex model that accounts for the observed substructure could help provide an explanation for the kinematic structure that McConnachie et al. (2006) observe.

Other authors have claimed M33 halo detections; Chandar et al. (2002) and Sarajedini et al. (2006) present evidence for distinct populations of star clusters and RR Lyrae, respectively, in M33. For the former, the older clusters are suggested to belong to

two kinematic components (a disk and a halo), whereas the younger clusters are consistent with belonging to only one component (a disk). For the latter, examination of the reddening and period distribution of individual stars suggests a bimodal population, with the less extincted, longer period (more metal-poor) stars attributed to a halo population. These studies are based on observations at much smaller radii than probed here ($< 0.5^\circ$ from the center of M33), and their interpretations are unlikely to be affected by the presence of this new substructure.

4.2. Origin of the M33 substructure

4.2.1. *An accreted dwarf galaxy?*

The luminosity of the structure surrounding the M33 disk is at least $M_V = -12.7 \pm 0.5$, similar to the integrated luminosity of a bright Local Group dwarf spheroidal, such as Fornax or Andromeda II. Further, with an estimated median photometric metallicity of $[Fe/H] = -1.6$ dex, it would be consistent with the broad luminosity - metallicity correlation that is observed for dwarf galaxies. If the M33 substructure is a tidal stream from a dwarf galaxy, then it is reasonable to ask if the progenitor is visible.

Only one dwarf satellite has been observed in the PAndAS footprint around M33 (excluding the previously known Andromeda II dwarf galaxy at the edge of the survey region), the low luminosity Andromeda XXII ($M_V \simeq -6$; Martin et al. 2009). There is no reason to suspect it as the progenitor of the substructure, given that it lies far out near the southern minor axis away from the main body of the feature. Likewise, Andromeda II shows no connection to the substructure, and anyway it is a relatively bright galaxy that does not show any sign of distortions (e.g., McConnachie et al. 2007). We cannot rule out the possibility that either the putative progenitor is entirely destroyed, or that it lies

directly in front or behind the main disk of M33.

4.2.2. *A tidal distortion due to M31?*

Our favored interpretation of the large substructure in M33 is that it is due to a tidal interaction with M31. A preliminary exploration of this idea was presented in McConnachie et al. (2009), and Dubinski et al. (2010, in preparation) develop this model. Here, we summarize a few salient points.

Morphology

Perhaps the most convincing piece of evidence for a tidal origin is the morphology of the feature. Although slightly asymmetric, it has a classical “S-shaped” appearance typical of a system that is tidally interacting with a more massive companion, and it resembles an extremely warped stellar disk. While the disruption of a dwarf galaxy is plausible, most orbits for the putative progenitor would not naturally produce a structure with the observed morphology.

Rogstad et al. (1976) first demonstrated that the HI disk of M33 was highly warped, and this has since been verified by Corbelli & Schneider (1997) and Putman et al. (2009). As such, it is perhaps unsurprising to find that the stellar disk is similarly perturbed. M. Putman kindly provided us with her group’s integrated HI map of M33 observed as part of the Galactic Arecibo L-Band Feed Array HI (GALFA-HI) Survey. Following Figure 1 of Putman et al. (2009), the left panel of Figure 17 shows the integrated HI contours of M33, where contour levels are $8.3 \times 1.5^n \times 10^{18} \text{ cm}^{-2}$ ($n = 0 \dots 13$). The middle panels shows a simple model of the disk of M33, using the variation in position angle and inclination derived by Corbelli & Schneider (1997). Here, we have modeled the density of the disk in

three dimensions by an exponential-sech² function, and integrated along the line of sight. Contours represent one magnitude drops in surface brightness from the maximum surface brightness of the disk. The right panel shows the observed surface brightness distribution map of M33, previously shown in Figure 13. Figure 17 shows that the stars and gas warp in the same direction, and both are reasonably well matched by the simple model of Corbelli & Schneider (1997). While such a similarity could be coincidence, it is also qualitative evidence for a common origin.

Metallicity

The analysis in Figure 10 shows that the MDF of the disk stars in the D1 annulus has a broadly similar IQR as the stellar substructure. However, the latter has a higher mean metallicity - by about 0.3 dex - than the disk population, and the peak metallicities of the two populations differ by ~ 0.6 dex. Comparison of the two Hess diagrams in Figure 11 shows that the two RGB populations are similar at the blue end but that the disk population has a significant redward extension that is absent in the substructure population. Given these differences, can the substructure be related to the disk population?

It is difficult to reconcile the differences between the CMDs and photometric MDFs of the substructure and disk fields with the data presented herein. We note that metallicity gradients have been observed in the M33 disk using a range of tracers (e.g., AGB stars, Cioni 2009; PNe, Magrini et al. 2009; Figure 20 of Barker et al. 2007 and references therein). Tiede et al. (2004) measure a gradient of $\Delta[\text{Fe}/\text{H}]/\Delta R_{\text{proj}} = -0.06 \pm 0.01 \text{ dex kpc}^{-1}$, based on the color of RGB stars, but so far no studies have probed the disk at radii close to that of the substructure studied here (~ 12 disk scale-lengths, using the estimate by Regan & Vogel 1994, measured in the J band). This is the very outer, very low surface brightness part of the disk, where few if any constraints exist on the intrinsic population of disks. If an

interaction has taken place, then this may well act to radially redistribute stars and gas, which will introduce and/or reshape gradients in age and metallicity, further complicating matters. Systematic gradients in age are particularly difficult for photometric-based analyses to account for, and spectroscopic metallicity studies will be required to better understand the population differences that this photometric study reveals.

Other considerations

The preliminary models of a tidal encounter between M31 and M33 presented in McConnachie et al. (2009) demonstrate that a relatively close interaction between M31 and M33 can plausibly produce a stellar feature on the scale observed, while also satisfying the known phase-space constraints of these galaxies (including the proper motion of M33; Brunthaler et al. 2005). Such an interaction may also affect other tracers in the outer regions of M33. For example, M33 appears to lack a significant population of globular clusters at larger radii; Huxor et al. (2009) discover four M33 globular clusters beyond the $\mu_B = 25 \text{ mag arcsec}^{-2}$ isophote, bringing the total beyond this radius to only five (including the extended remote globular cluster discovered by Stonkutė et al. 2008). All but the least remote of these clusters are in the hemisphere of M33 furthest from M31, which Huxor et al. (2009) suggest may be tentative signs of tidal disturbance in M33 at large radius.

Another useful tracer of galaxies at large radii are planetary nebulae (PNe). Ciardullo et al. (2004) conduct a survey of the PNe population of M33 over the entire main disk of M33. They find that the velocity dispersion does not decrease over ~ 4 disk scale-lengths and has a value of nearly $\sigma \simeq 20 \text{ km s}^{-1}$ at $\sim 10 \text{ kpc}$ from the center of the galaxy. One possible explanation for this behavior is that the outer PNe have been dynamically heated due to tidal interactions with M31. Similarly, the study by M06 measure a velocity dispersion of the M33 disk at $\sim 9 \text{ kpc}$ of $\sim 12.5 \text{ km s}^{-1}$, higher than

expected from simple dynamical arguments, and again consistent with the idea of tidal heating. Finally, Putman et al. (2009) also measure high velocity dispersion for the HI across the disk of M33, which they suggest may be consistent with a recent interaction with M31.

5. Summary

In this paper we have presented an analysis of g and i photometry of approximately 40 square degrees surrounding M33, taken as part of the PAndAS program using the MegaPrime/MegaCam instrument on CFHT. We show that the large stellar structure surrounding M33, first identified by McConnachie et al. (2009), is broadly aligned with the warped HI disk of M33 (Rogstad et al. 1976; Corbelli & Schneider 1997; Putman et al. 2009). We trace this feature to $\mu_V \simeq 33 \text{ mags arcsec}^{-2}$ and show that it extends to projected radii of $\sim 40 \text{ kpc}$ from the center of M33 in both the north-west and south-east quadrants of the galaxy, giving the structure an “S’-shaped” appearance. Its stellar populations are consistent with an old population with $\langle [Fe/H] \rangle \sim -1.6 \text{ dex}$ and an interquartile range in metallicity of 0.5 dex. We calculate a lower limit to the integrated luminosity of the structure of $-12.7 \pm 0.5 \text{ mags}$, comparable to a bright dwarf galaxy such as Fornax or Andromeda II and slightly less than 1% of the total luminosity of M33. We show that there is tentative evidence for a distortion in the distribution of young stars near the edge of the HI disk that occurs at similar azimuth to the warp in HI. These data also hint at an extended halo component that dominates at very large radius and which will be explored in detail in a forthcoming contribution. We revisit studies of M33 and its stellar populations in light of these new results, and we discuss possible formation models for the vast stellar structure. Our favored scenario is the tidal disruption of M33 as it orbits around M31.

Based on observations obtained with MegaPrime/MegaCam, a joint project of CFHT and CEA/DAPNIA, at the Canada-France-Hawaii Telescope (CFHT) which is operated by the National Research Council (NRC) of Canada, the Institut National des Sciences de l'Univers of the Centre National de la Recherche Scientifique of France, and the University of Hawaii. We would like to thank the entire staff at CFHT for their great efforts and continuing support throughout this project. We thank Mary Putman for supplying us with the integrated HI column density map for M33 and for comments on the manuscript. Thanks to all our collaborators in the PAndAS, particularly Scott Chapman, Mark Fardal, Nicolas Martin and Jorge Peñarrubia, for a careful reading of the manuscript and thoughtful comments, and finally to the anonymous referee, for useful comments that improved this paper. A.M.N.F. acknowledge support by a Marie Curie Excellence Grant from the European Commission under contract MCEXT-CT-2005-025869.

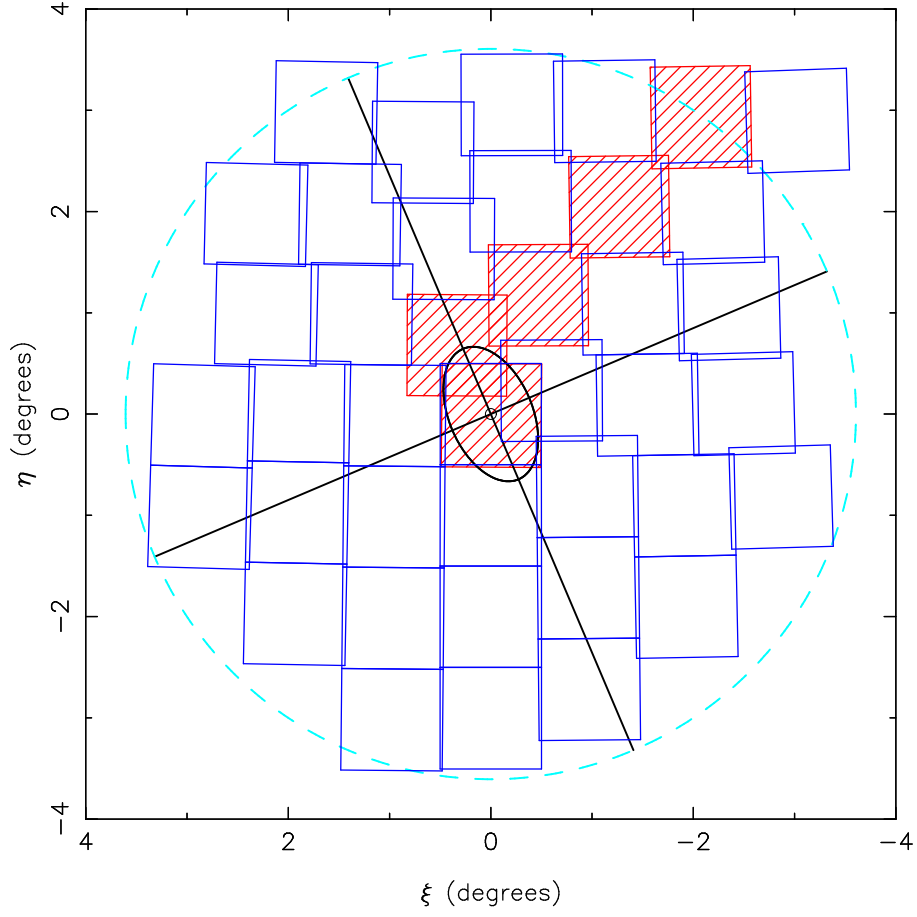


Fig. 1.— A tangent plane projection of the location of 40 PAndAS fields in the vicinity of M33. The ellipse marks the radius at which $\mu_B \simeq 25 \text{ mag arcsec}^{-2}$. Major and minor axes are shown. The dashed circle corresponds to a projected radius of 50 kpc from M33. Hatched fields were presented in Ibata et al. (2007). Open fields were observed in S08B.

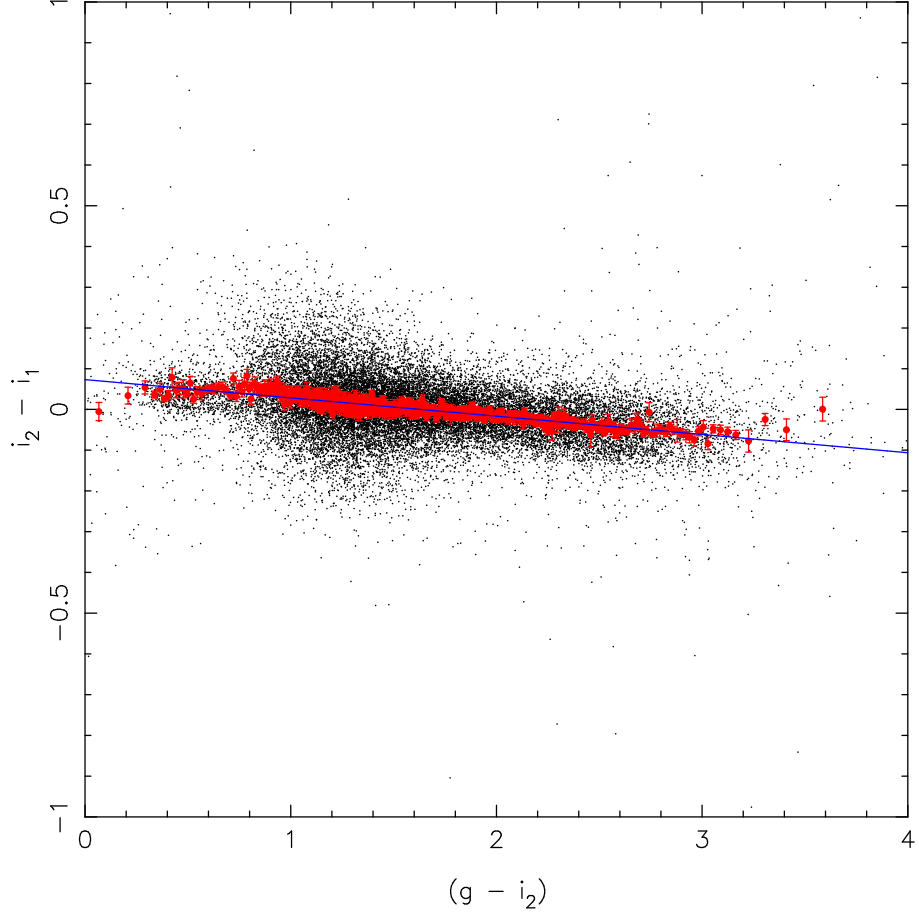


Fig. 2.— The difference between the old (i_2) and new (i_1) CFHT/MegaPrime i filter (pre- and post-2007, respectively) as a function of color $(g - i_2)$ using stellar sources in regions where we have overlap between the two generations of i -filters. Red points and their error bars show the mean and variance in bins containing 50 stellar sources. The straight line shows the best fit linear relation, described by Equation 1.

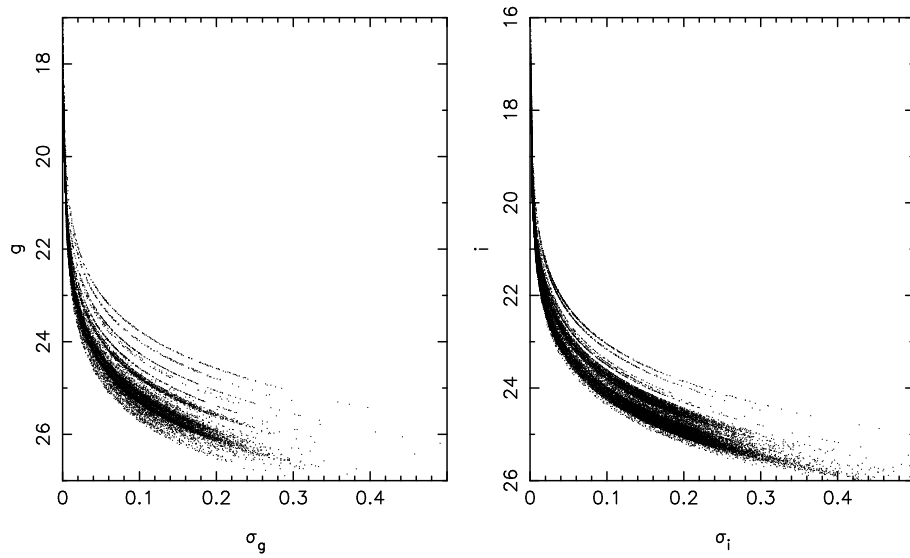


Fig. 3.— Photometric errors as a function of magnitude. The distinct sequences are due to fields that were taken in slightly different observing conditions. Generally, our photometry is accurate to better than 0.2 mags for $i \leq 24.5$ and $g \leq 25.5$.

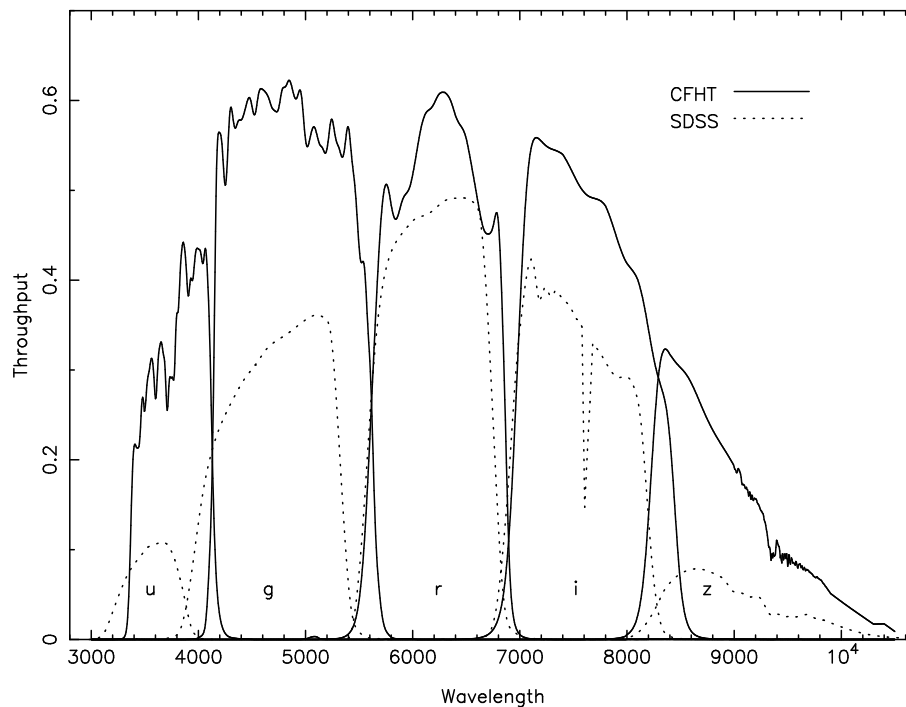


Fig. 4.— A comparison of the SDSS and CFHT filter transmission curves, taking into account the throughput of the telescope optics, the quantum efficiency of the CCDs, and the atmospheric transmission curves. The CFHT *g* filter is shifted to the red in comparison the SDSS equivalent, and the CFHT *i* filter is broader than the SDSS equivalent by $\sim 250\text{\AA}$ towards the red end of the spectrum.

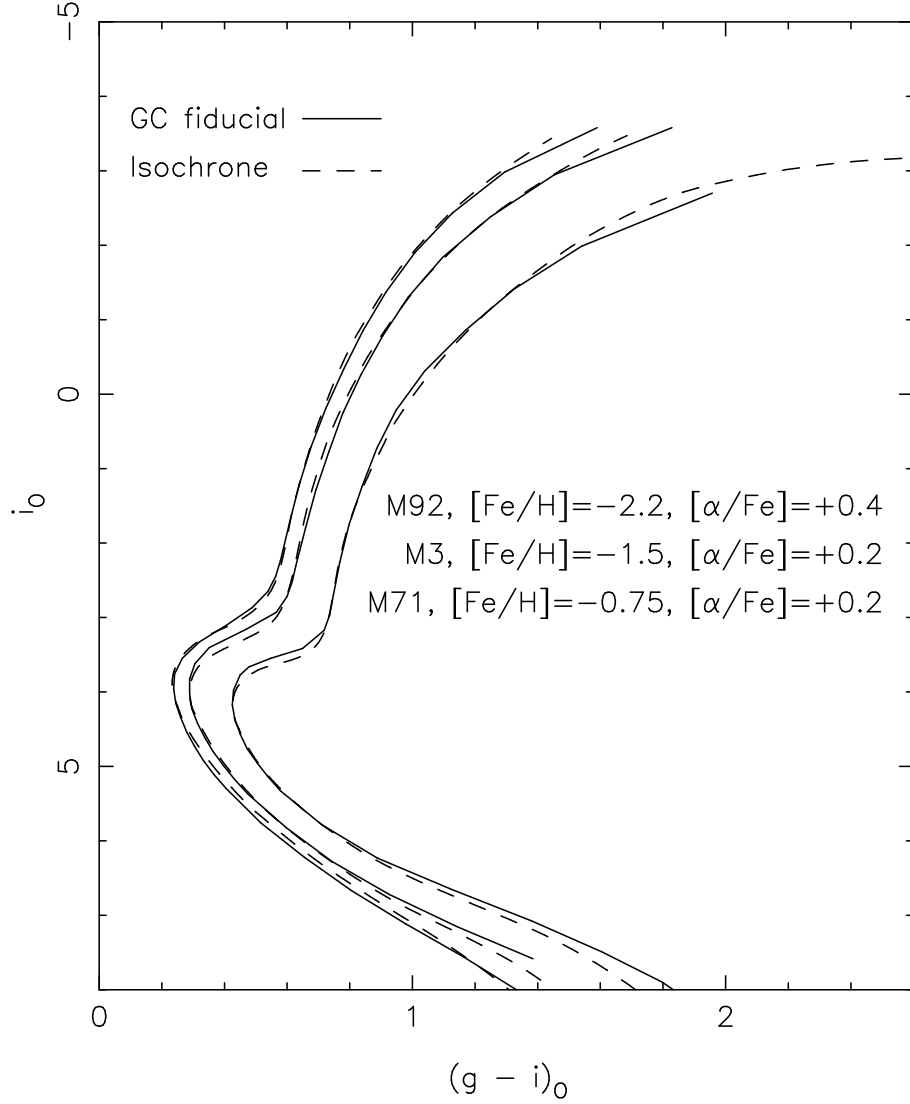


Fig. 5.— A comparison of the CFHT isochrones for 14Gyr populations (dashed lines) to fiducial sequences for the globular clusters M92, M3 and M71 taken from Clem et al. (2008) (solid lines). The key denotes the $[\text{Fe}/\text{H}]$ and $[\alpha/\text{Fe}]$ used for each cluster. The assumed distance moduli and $E(B-V)$ values for the clusters are given in the text. Clearly, the isochrones match the fiducial sequences very well. Only the giant branch of the isochrones will be required for the subsequent analysis.

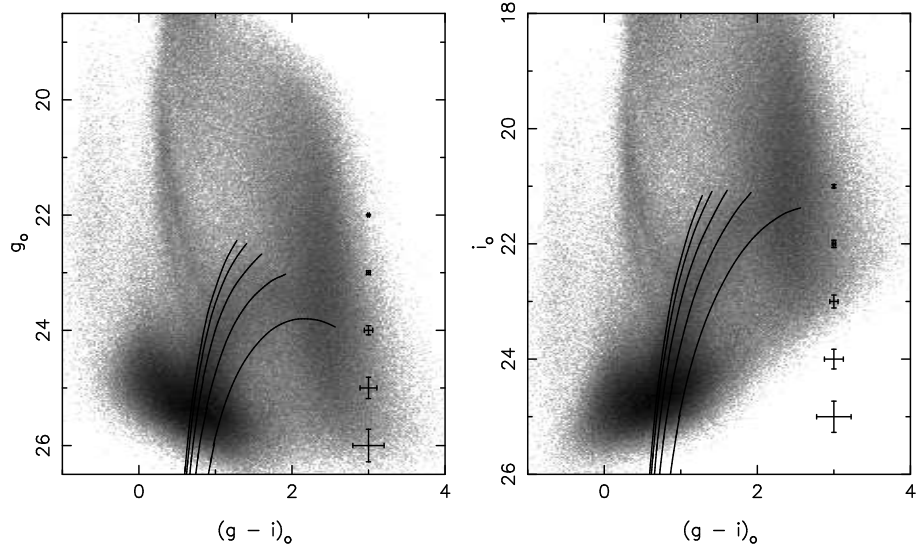


Fig. 6.— g_o (left) and i_o (right) color-magnitude (Hess) diagrams of all stellar objects in the M33 survey region shown in Figure 1, excluding the central field. Bins are 0.025×0.025 mags, displayed with a logarithmic scaling. Mean errors as a function of magnitude are shown. Overlaid are isochrones corresponding to a 12 Gyr, $[\alpha/\text{Fe}] = 0.0$, stellar population at the distance of M33 with $[Fe/H] = -2.5, -2, -1.5, -1$ and -0.5 dex.

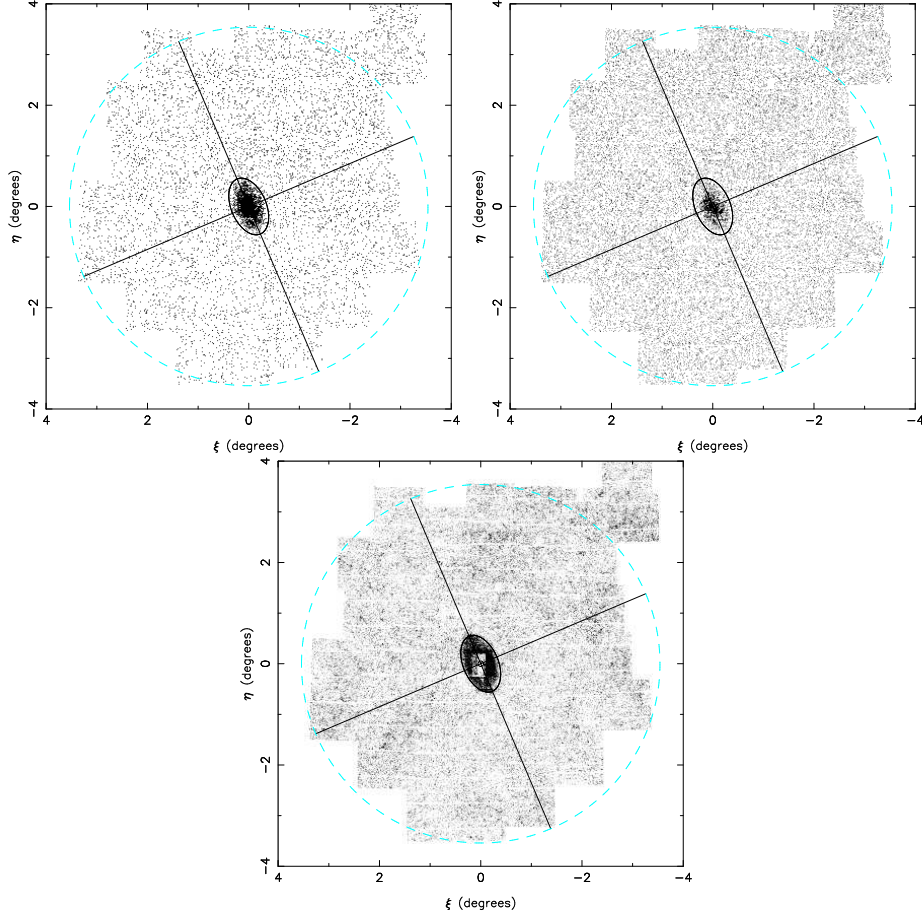


Fig. 7.— The spatial distribution of various contaminants in our photometric survey of M33. Maps use 1.2×1.2 arcmins pixels and are displayed with a linear scale. Left panel: Galactic halo stars, selected to have $19.0 < i_0 < 22.0$, $0.1 < (g - i)_0 < 0.6$. Middle panel: Galactic disk stars, selected to have $17.0 < i_0 < 20.0$, $1.5 < (g - i)_0 < 3.0$. Right panel: extended sources (galaxies) with $17.0 < i_0 < 23.5$. Faint, compact galaxies misidentified as stars are likely to have a similar spatial distribution to the latter population.

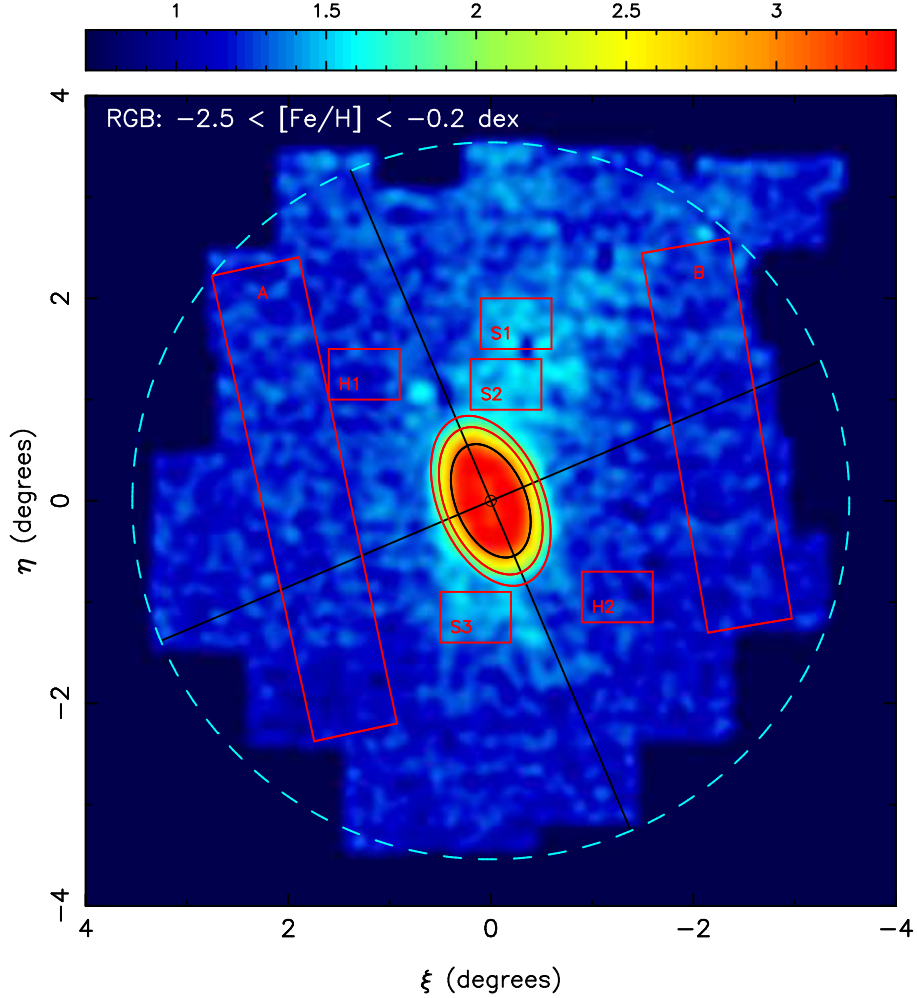


Fig. 8.— The spatial distribution of candidate RGB stars at the distance of M33 with $i_0 \leq 23.5$ in a tangent-plane projection displayed with logarithmic scaling. These stars lie in the same color - magnitude locus as 12 Gyrs, $[\alpha/Fe] = 0.0$, isochrones, with metallicities between $-2.5 \leq [Fe/H] \leq -0.2$ dex, shifted to the distance modulus of M33. A slight gradient from north to south is visible, since the more metal-rich RGB stars overlap in color-magnitude space with the foreground disk population. The small red boxes and the red elliptical annulus each have an area of 0.35 square degrees and probe areas of interest around M33. The large rectangular strips, A and B, each probe 1 degree strips in Galactic latitude away from the main body of M33 and are used later to examine variations in the Galactic foreground (see text for details).

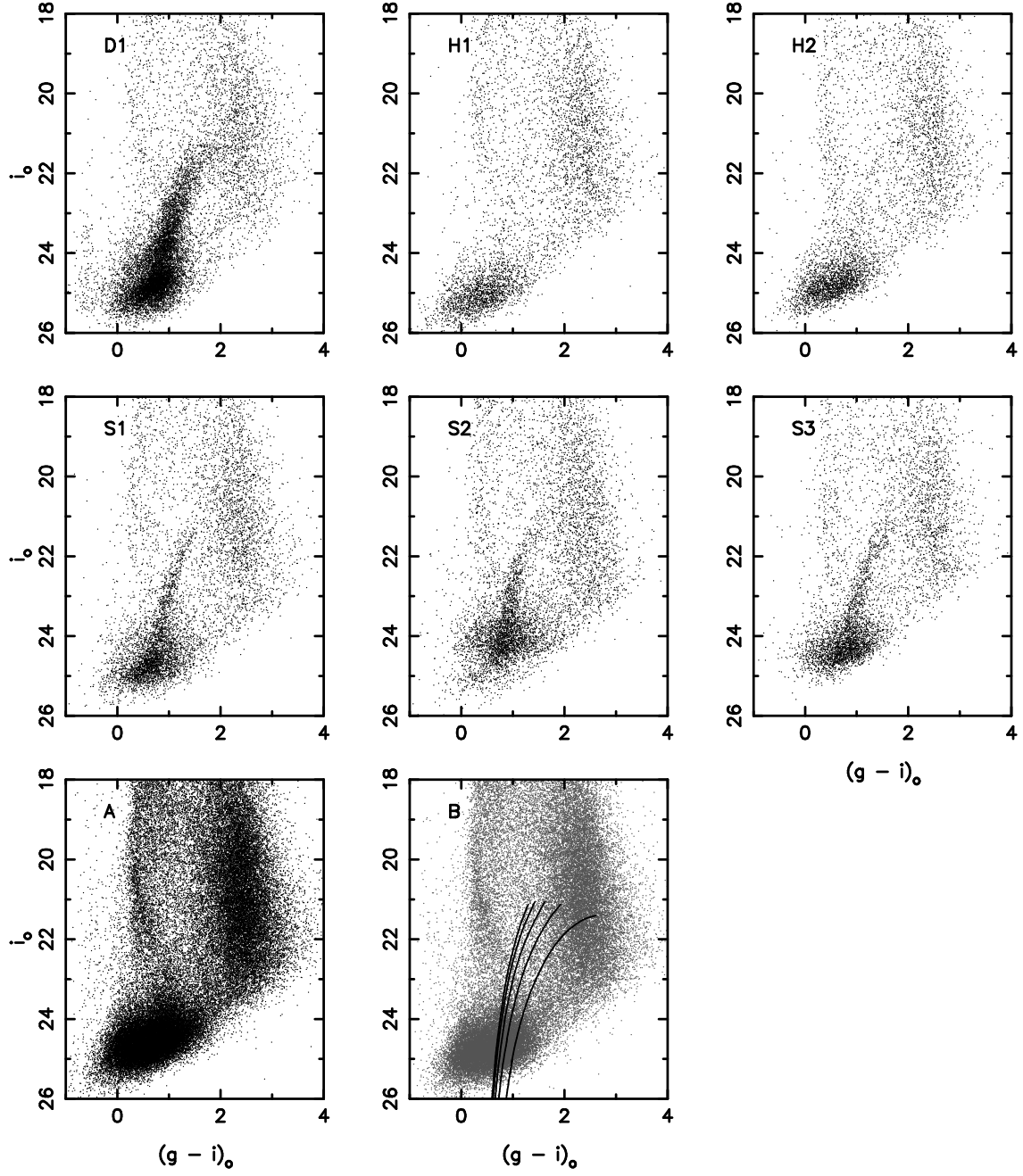


Fig. 9.— i -band CMDs of the areas highlighted in Figure 8. Field D1 (corresponding to the elliptical annulus) samples stars in the outer disk of M33; H1 and H2 sample areas away from obvious substructure and are putative “halo” fields; S1, S2 and S3 sample the substructure around the disk of M33 at similar radii to the halo fields. Each of these field has the same area (0.35 square degrees). CMDs for area A and B are also shown, and isochrones corresponding to $[\text{Fe}/\text{H}] = -0.5, -1.0, -1.5, -2.0, -2.5$ dex are overlaid on area B for reference.

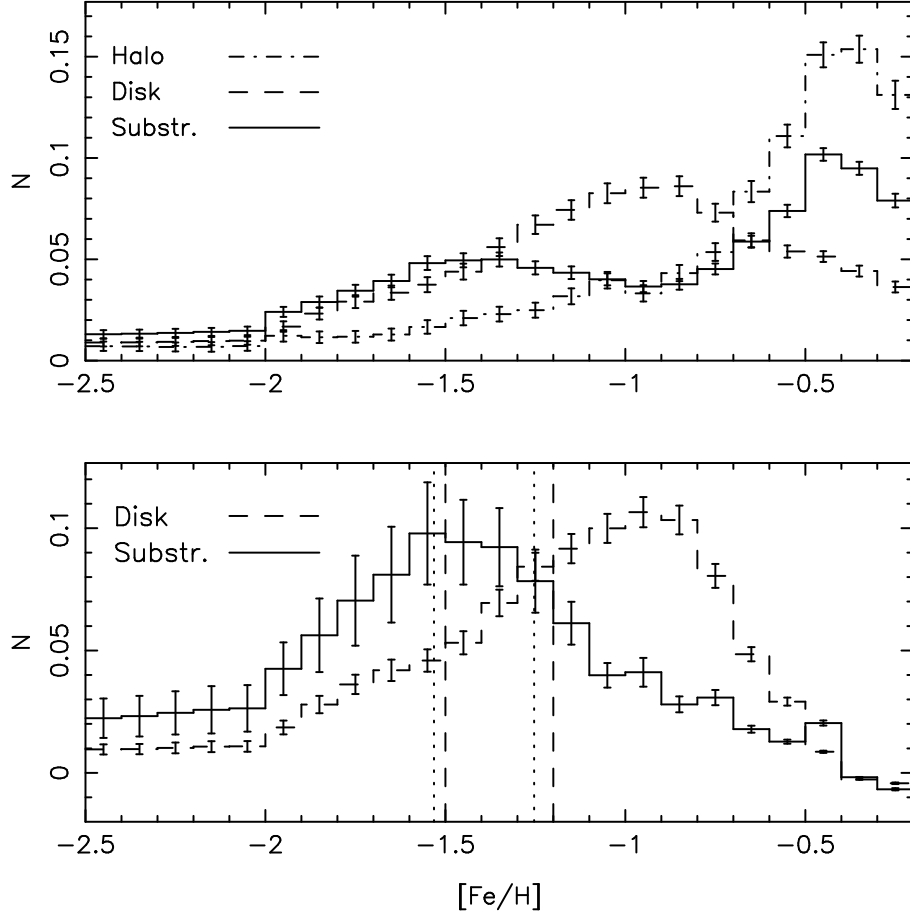


Fig. 10.— Upper panel: The photometric metallicity distribution functions (MDFs) for the combined putative halo fields (H1 and H2; dot-dashed histogram), disk annulus field (D1; dashed histogram) and the combined substructure fields (S1, S2 and S3; solid histogram), uncorrected for foreground contamination, and scaled to have unity area under the curves. These were derived by bilinear interpolation of 12Gyr isochrones for candidate RGB stars with $i_o \leq 23.5$ (see text for details). Lower panel: Corrected MDFs for the substructure and disk fields (solid and dashed histograms, respectively), after subtraction of the “halo” MDF, suitably scaled. Dotted and dot-dashed vertical lines correspond to mean and median metallicities (respectively) for each MDF.

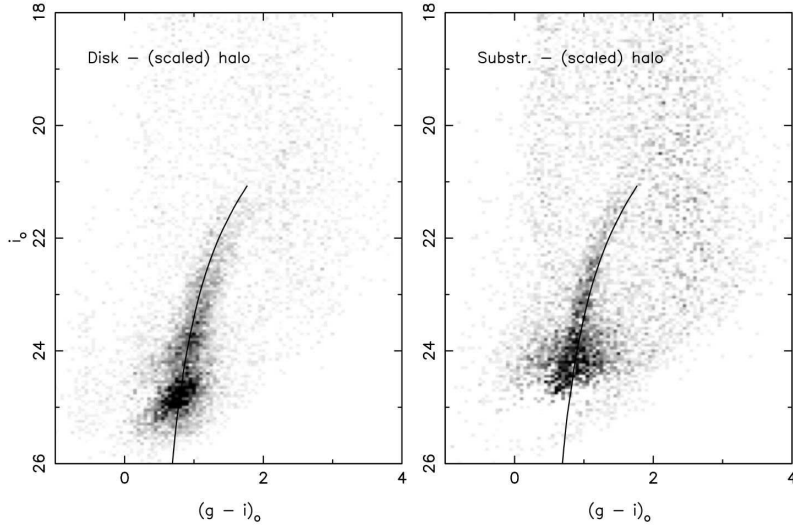


Fig. 11.— Background-corrected Hess diagrams for the disk (left panel) and combined substructure (right panel) fields. Here, the combined “halo” fields have been subtracted from the disk and substructure Hess diagrams using the same scaling as for the MDFs in the lower panel of Figure 10. Pixels are 0.05×0.05 mags, and for clarity only positive residuals are shown on a linear scale. A 12Gyr, $[\alpha/Fe] = 0.0$, $[Fe/H] = -1.2$ dex isochrones (the mean metallicity of the disk field) is overlaid in both panels for reference.

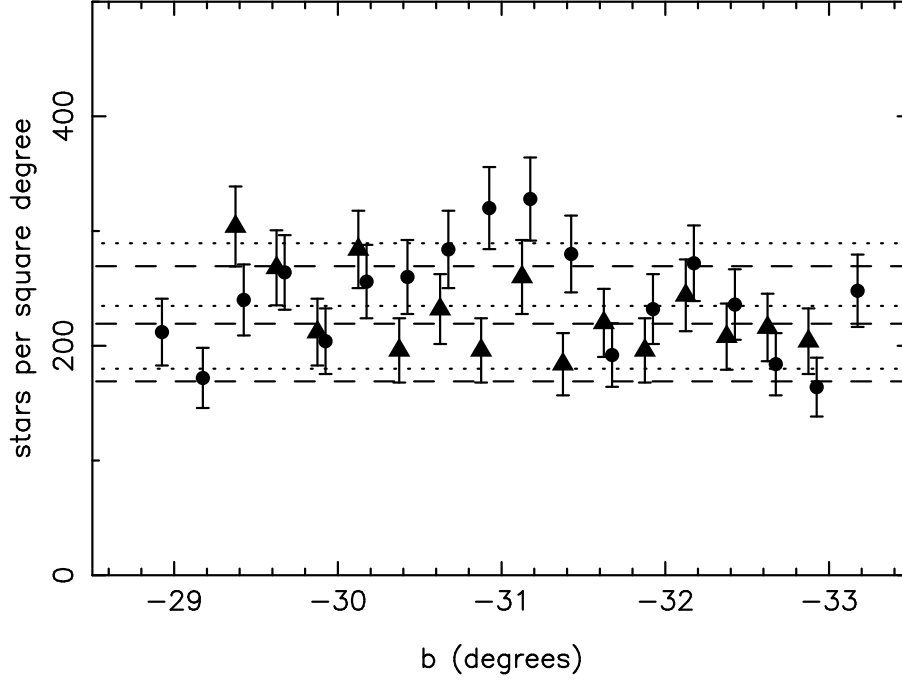


Fig. 12.— Number density of stars as a function of galactic latitude (b) in strip A (circles) and strip B (triangles), in the RGB photometric metallicity interval $-2.0 \leq [\text{Fe}/\text{H}] \leq -1.0$ dex. Most of these stars are expected to be Galactic foreground stars, and not genuine RGB stars in M33. Dotted and dashed lines show the mean and 1σ spreads for strips A and B, respectively. In this metallicity interval, the foreground contamination does not vary significantly between strips or with latitude.

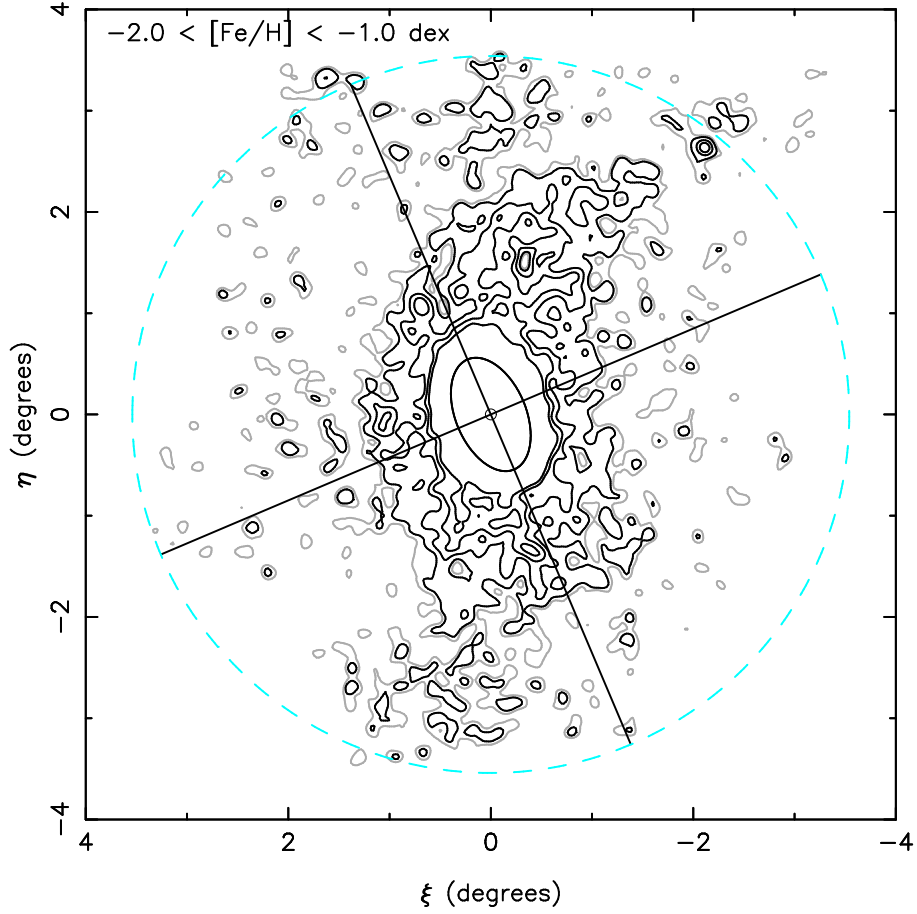


Fig. 13.— The density distribution of candidate RGB stars in the metallicity interval $-2.0 \leq [\text{Fe}/\text{H}] \leq -1.0$ dex, using an identical procedure to Figure 8. This metallicity cut was selected to optimally identify the M33 substructure. Black contours are 2, 5, 8 and 12σ above the background, corresponding to estimated surface brightness limits of $\mu_V = 32.5, 31.7, 31.2$ and $30.6 \text{ mag arcsec}^{-2}$, respectively. The gray contour is 1σ above the background ($\mu_V \simeq 33.0 \text{ mag arcsec}^{-2}$).

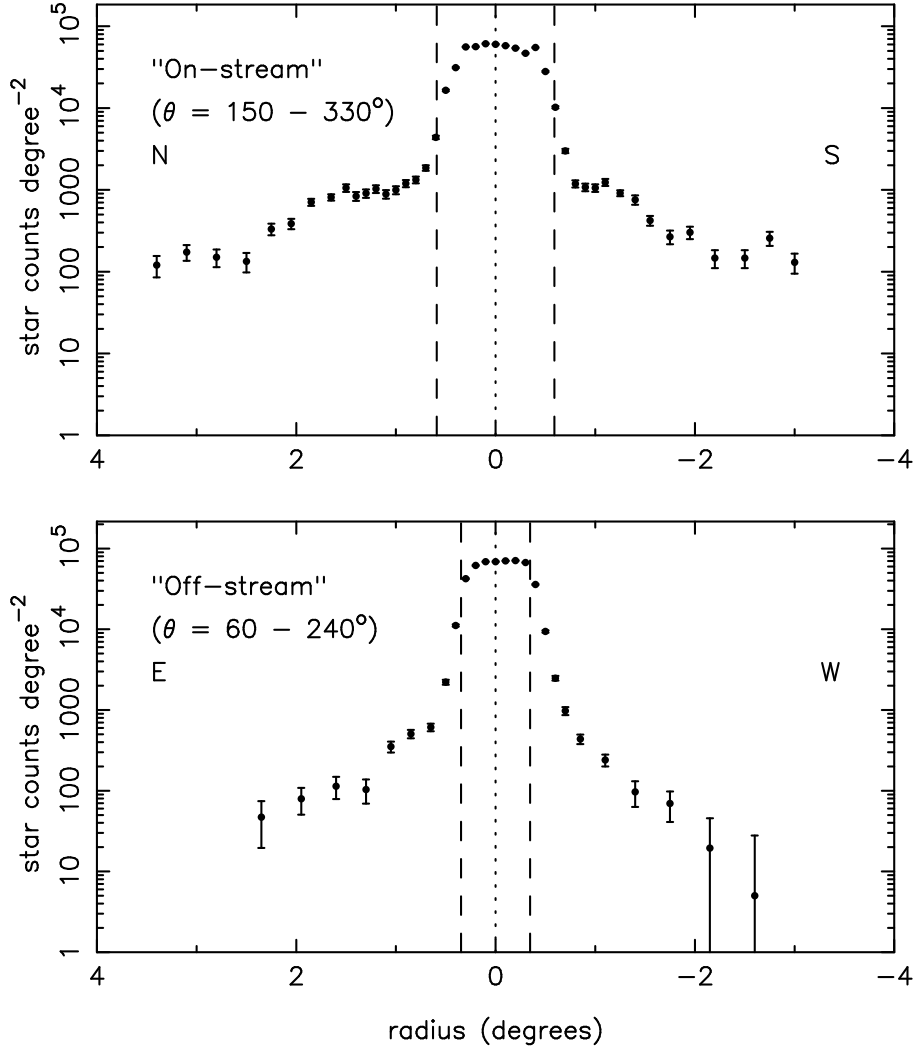


Fig. 14.— The radial profile of M33, constructed in 1 degree wide strips, in two orthogonal directions, using identical cuts as for Figure 13. The top panel shows the radial profile in an “on-stream” region, and the bottom panel shows the profile in an “off-stream” region. Here, θ refers to an angle, east-from-north, where $\theta = 0$ corresponds to the northern major axis of M33. Dashed lines correspond to the radius of the $\mu_B = 25 \text{ mag arcsec}^{-2}$ isophote. The extended structure is clearly visible in the top panel, and can also clearly be seen in the east in the lower panel. At larger radius in the lower panel, there are hints of a slowly declining component, presumably a M33 halo component.

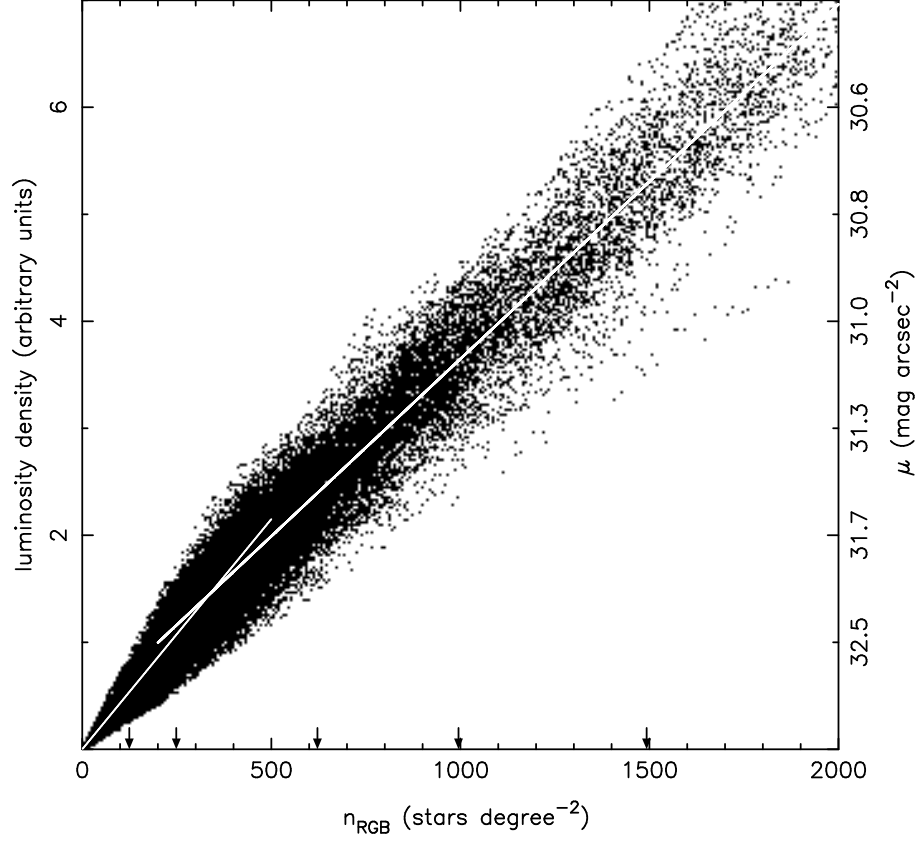


Fig. 15.— Relation between number density of RGB stars and luminosity density for Figure 13. The surface brightness scale on the right vertical axis is calculated using the transformation derived from Andromeda I. Arrows indicate values of 1, 2, 5, 8, and 12 σ contours shown in Figure 13. See text for details.

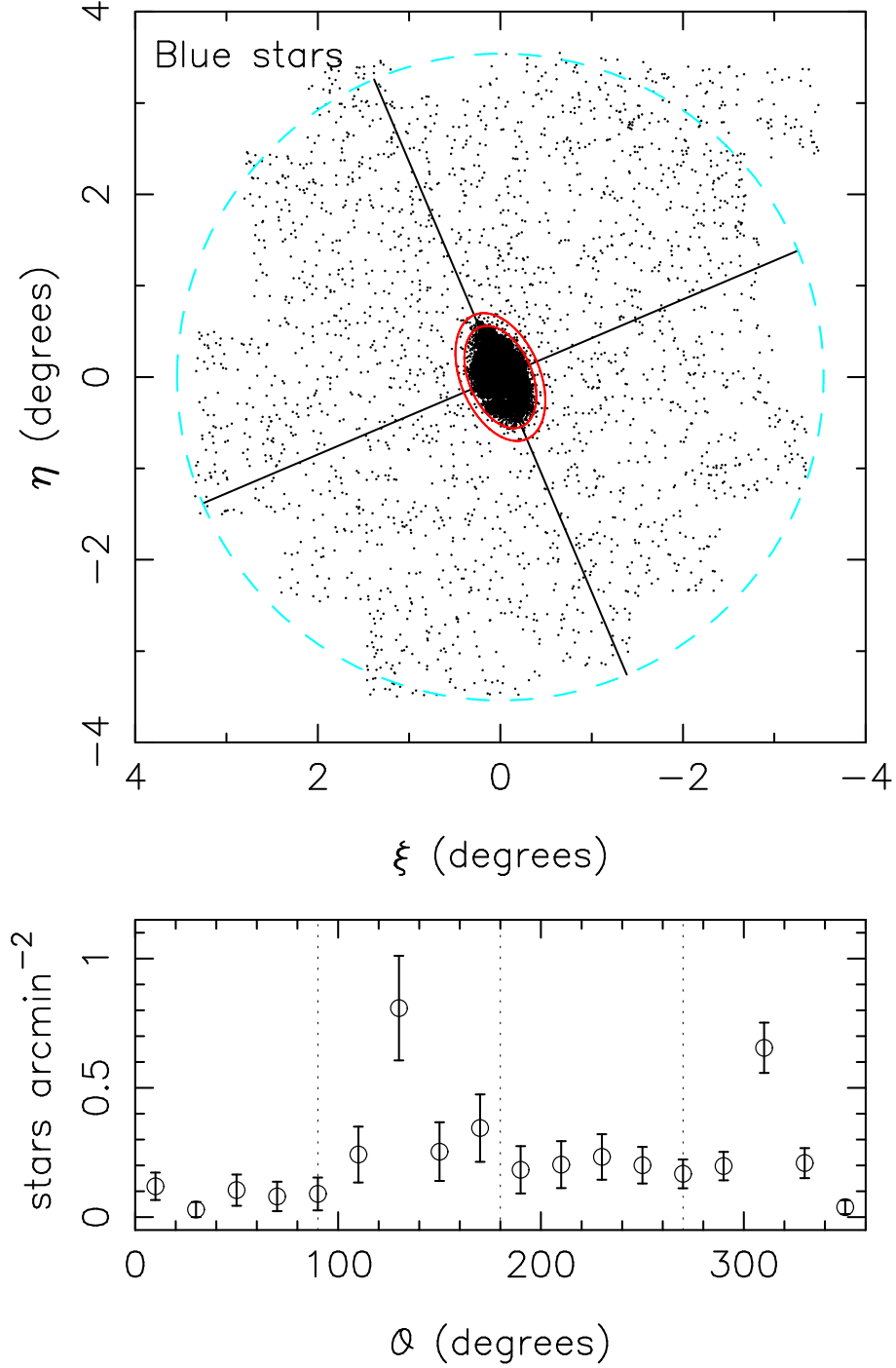


Fig. 16.— Upper panel: Tangent plane projection of the location of young, blue stars in M33, defined by $(g - i)_o < 0.0$ and $i_o < 23.5$. An annulus in the outer disk is highlighted. Lower panel: Circular points show the density distribution of young stars in the annulus highlighted in the upper panel as a function of azimuth, where $\theta = 0$ corresponds to the northern semi-major axis and $\theta = 90^\circ$ corresponds to the eastern semi-minor axis.

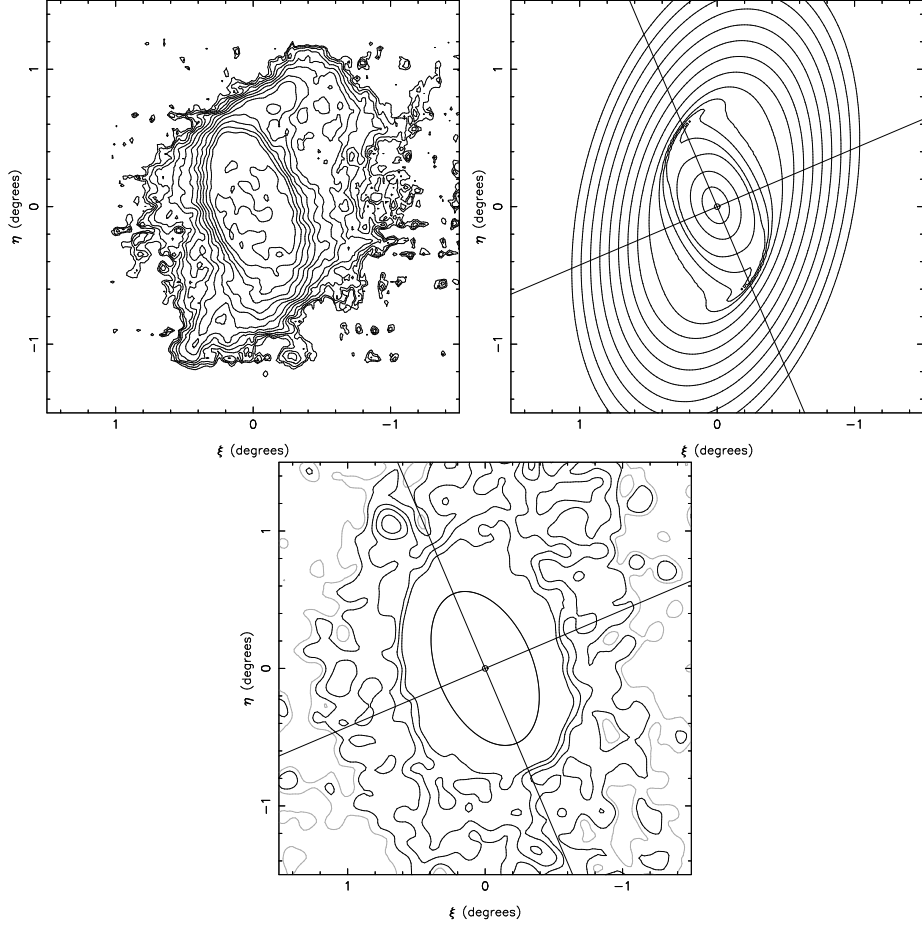


Fig. 17.— Left panel: M33 HI integrated column density, reproduced from Figure 1 of Putman et al. (2009). Contour levels are $8.3 \times 1.5^n \times 10^{18} \text{ cm}^{-2}$ with $n = 0 \dots 13$. The lowest contour level is a 5σ detection threshold to a 25 km s^{-1} feature. Middle panel: Simple model of the M33 disk using the ring model of Corbelli & Schneider (1997) for position and inclination as a function of r . Contour levels correspond to 1 magnitude intervals in surface brightness. Right panel: The M33 stellar substructure surface brightness map. Contours are the same as Figure 13; the highest surface brightness contour has $\mu_V \simeq 30.7 \text{ mags arcsec}^{-2}$ (Table 1).

$\mu_V \text{ mag arcsec}^{-2}$		
Level (σ)	And I scale	And III scale
1	32.8 (33.2)	32.9 (33.3)
2	32.3 (32.4)	32.5 (32.5)
5	31.6 (31.4)	31.7 (31.6)
8	31.1 (30.9)	31.2 (31.0)
12	30.7 (30.5)	30.8 (30.6)

Table 1: Conversions between contour levels in the stellar density map (Figure 13) to surface brightness thresholds for different empirical transformations. See text for details.

REFERENCES

- Barker, M. K., Sarajedini, A., Geisler, D., Harding, P., & Schommer, R. 2007, *AJ*, 133, 1125
- Bohlin, R. C. 2007, in *Astronomical Society of the Pacific Conference Series*, Vol. 364, *The Future of Photometric, Spectrophotometric and Polarimetric Standardization*, ed. C. Sterken, 315
- Bonanos, A. Z., Stanek, K. Z., Kudritzki, R. P., Macri, L. M., Sasselov, D. D., Kaluzny, J., Stetson, P. B., Bersier, D., Bresolin, F., Matheson, T., Mochejska, B. J., Przybilla, N., Szentgyorgyi, A. H., Tonry, J., & Torres, G. 2006, *ApJ*, 652, 313
- Bothun, G. D. 1992, *AJ*, 103, 104
- Brunthaler, A., Reid, M. J., Falcke, H., Greenhill, L. J., & Henkel, C. 2005, *Science*, 307, 1440
- Chandar, R., Bianchi, L., Ford, H. C., & Sarajedini, A. 2002, *ApJ*, 564, 712
- Chapman, S. C., Ibata, R., Lewis, G. F., Ferguson, A. M. N., Irwin, M., McConnachie, A., & Tanvir, N. 2006, *ApJ*, 653, 255
- Chiba, M. & Beers, T. C. 2000, *AJ*, 119, 2843
- Ciardullo, R., Durrell, P. R., Laychak, M. B., Herrmann, K. A., Moody, K., Jacoby, G. H., & Feldmeier, J. J. 2004, *ApJ*, 614, 167
- Cioni, M. 2009, *A&A*, 506, 1137
- Clem, J. L., Vanden Berg, D. A., & Stetson, P. B. 2008, *AJ*, 135, 682
- Corbelli, E. 2003, *MNRAS*, 342, 199
- Corbelli, E. & Salucci, P. 2000, *MNRAS*, 311, 441

- Corbelli, E. & Schneider, S. E. 1997, *ApJ*, 479, 244
- Da Costa, G. S., Armandroff, T. E., & Caldwell, N. 2002, *AJ*, 124, 332
- Da Costa, G. S., Armandroff, T. E., Caldwell, N., & Seitzer, P. 1996, *AJ*, 112, 2576
- Dotter, A., Chaboyer, B., Jevremović, D., Baron, E., Ferguson, J. W., Sarajedini, A., & Anderson, J. 2007, *AJ*, 134, 376
- Dotter, A., Chaboyer, B., Jevremović, D., Kostov, V., Baron, E., & Ferguson, J. W. 2008, *ApJS*, 178, 89
- Ferguson, A., Irwin, M., Chapman, S., Ibata, R., Lewis, G., & Tanvir, N. 2007, *Resolving the Stellar Outskirts of M31 and M33 (ISLAND UNIVERSES, Astrophysics and Space Science Proceedings. ISBN 978-1-4020-5572-0. Springer, 2007, p. 239)*, 239
- Ferguson, A. M. N., Irwin, M. J., Ibata, R. A., Lewis, G. F., & Tanvir, N. R. 2002, *AJ*, 124, 1452
- Galletti, S., Bellazzini, M., & Ferraro, F. R. 2004, *A&A*, 423, 925
- Girardi, L., Grebel, E. K., Odenkirchen, M., & Chiosi, C. 2004, *A&A*, 422, 205
- Huxor, A., Ferguson, A. M. N., Barker, M. K., Tanvir, N. R., Irwin, M. J., Chapman, S. C., Ibata, R., & Lewis, G. 2009, *ApJ*, 698, L77
- Ibata, R., Irwin, M., Lewis, G., Ferguson, A. M. N., & Tanvir, N. 2001, *Nature*, 412, 49
- Ibata, R., Martin, N. F., Irwin, M., Chapman, S., Ferguson, A. M. N., Lewis, G. F., & McConnachie, A. W. 2007, *ApJ*, 671, 1591
- Irwin, M. & Lewis, J. 2001, *New Astronomy Review*, 45, 105

- Irwin, M. J., Ferguson, A. M. N., Huxor, A. P., Tanvir, N. R., Ibata, R. A., & Lewis, G. F. 2008, *ApJ*, 676, L17
- Irwin, M. J., Ferguson, A. M. N., Ibata, R. A., Lewis, G. F., & Tanvir, N. R. 2005, *ApJ*, 628, L105
- Kalirai, J. S., Gilbert, K. M., Guhathakurta, P., Majewski, S. R., Ostheimer, J. C., Rich, R. M., Cooper, M. C., Reitzel, D. B., & Patterson, R. J. 2006, *ApJ*, 648, 389
- Magrini, L., Stanghellini, L., & Villaver, E. 2009, *ApJ*, 696, 729
- Martin, N. F., Ibata, R. A., & Irwin, M. 2007, *ApJ*, 668, L123
- Martin, N. F., Ibata, R. A., Irwin, M. J., Chapman, S., Lewis, G. F., Ferguson, A. M. N., Tanvir, N., & McConnachie, A. W. 2006, *MNRAS*, 371, 1983
- Martin, N. F., McConnachie, A. W., Irwin, M., Widrow, L. M., Ferguson, A. M. N., Ibata, R. A., Dubinski, J., Babul, A., Chapman, S., Fardal, M., Lewis, G. F., Navarro, J., & Rich, R. M. 2009, *ApJ*, 705, 758
- Mateo, M. L. 1998, *ARA&A*, 36, 435
- McConnachie, A. W., Arimoto, N., & Irwin, M. 2007, *MNRAS*, 379, 379
- McConnachie, A. W., Chapman, S. C., Ibata, R. A., Ferguson, A. M. N., Irwin, M. J., Lewis, G. F., Tanvir, N. R., & Martin, N. 2006, *ApJ*, 647, L25
- McConnachie, A. W., Huxor, A., Martin, N. F., Irwin, M. J., Chapman, S. C., Fahlman, G., Ferguson, A. M. N., Ibata, R. A., Lewis, G. F., Richer, H., & Tanvir, N. R. 2008, *ApJ*, 688, 1009
- McConnachie, A. W. & Irwin, M. J. 2006, *MNRAS*, 365, 902

- McConnachie, A. W., Irwin, M. J., Ferguson, A. M. N., Ibata, R. A., Lewis, G. F., & Tanvir, N. 2004a, MNRAS, 350, 243
- . 2005, MNRAS, 356, 979
- McConnachie, A. W., Irwin, M. J., Ibata, R. A., Dubinski, J., Widrow, L. M., Martin, N. F., Côté, P., Dotter, A. L., Navarro, J. F., Ferguson, A. M. N., Puzia, T. H., Lewis, G. F., Babul, A., Barmby, P., Bienaymé, O., Chapman, S. C., Cockcroft, R., Collins, M. L. M., Fardal, M. A., Harris, W. E., Huxor, A., Mackey, A. D., Peñarrubia, J., Rich, R. M., Richer, H. B., Siebert, A., Tanvir, N., Valls-Gabaud, D., & Venn, K. A. 2009, Nature, 461, 66
- McConnachie, A. W., Irwin, M. J., Ibata, R. A., Ferguson, A. M. N., Lewis, G. F., & Tanvir, N. 2003, MNRAS, 343, 1335
- McConnachie, A. W., Irwin, M. J., Lewis, G. F., Ibata, R. A., Chapman, S. C., Ferguson, A. M. N., & Tanvir, N. R. 2004b, MNRAS, 351, L94
- McLean, I. S. & Liu, T. 1996, ApJ, 456, 499
- Minniti, D., Olszewski, E. W., & Rieke, M. 1993, ApJ, 410, L79
- Purcell, C. W., Bullock, J. S., & Zentner, A. R. 2007, ApJ, 666, 20
- Putman, M. E., Peek, J. E. G., Muratov, A., Gnedin, O. Y., Hsu, W., Douglas, K. A., Heiles, C., Stanimirovic, S., Korpela, E. J., & Gibson, S. J. 2009, ApJ, 703, 1486
- Regan, M. W. & Vogel, S. N. 1994, ApJ, 434, 536
- Regnault, N., Conley, A., Guy, J., Sullivan, M., Cuillandre, J., Astier, P., Balland, C., Basa, S., Carlberg, R. G., Fouchez, D., Hardin, D., Hook, I. M., Howell, D. A., Pain, R., Perrett, K., & Pritchett, C. J. 2009, A&A, 506, 999

- Rejkuba, M., da Costa, G. S., Jerjen, H., Zoccali, M., & Binggeli, B. 2006, *A&A*, 448, 983
- Renzini, A. & Fusi Pecci, F. 1988, *ARA&A*, 26, 199
- Rocha-Pinto, H. J., Majewski, S. R., Skrutskie, M. F., Crane, J. D., & Patterson, R. J. 2004, *ApJ*, 615, 732
- Rogstad, D. H., Wright, M. C. H., & Lockhart, I. A. 1976, *ApJ*, 204, 703
- Sarajedini, A., Barker, M. K., Geisler, D., Harding, P., & Schommer, R. 2006, *AJ*, 132, 1361
- Schlegel, D. J., Finkbeiner, D. P., & Davis, M. 1998, *ApJ*, 500, 525
- Stonkutė, R., Vansevičius, V., Arimoto, N., Hasegawa, T., Narbutis, D., Tamura, N., Jablonka, P., Ohta, K., & Yamada, Y. 2008, *AJ*, 135, 1482
- Tiede, G. P., Sarajedini, A., & Barker, M. K. 2004, *AJ*, 128, 224
- U, V., Urbaneja, M. A., Kudritzki, R., Jacobs, B. A., Bresolin, F., & Przybilla, N. 2009, *ApJ*, 704, 1120
- Zucker, D. B., Kniazev, A. Y., Bell, E. F., Martínez-Delgado, D., Grebel, E. K., Rix, H., Rockosi, C. M., Holtzman, J. A., Walterbos, R. A. M., Annis, J., York, D. G., Ivezić, Ž., Brinkmann, J., Brewington, H., Harvanek, M., Hennessy, G., Kleinman, S. J., Krzesinski, J., Long, D., Newman, P. R., Nitta, A., & Snedden, S. A. 2004a, *ApJ*, 612, L121
- Zucker, D. B., Kniazev, A. Y., Bell, E. F., Martínez-Delgado, D., Grebel, E. K., Rix, H., Rockosi, C. M., Holtzman, J. A., Walterbos, R. A. M., Ivezić, Ž., Brinkmann, J., Brewington, H., Harvanek, M., Kleinman, S. J., Krzesinski, J., Lamb, D. Q., Long, D., Newman, P. R., Nitta, A., & Snedden, S. A. 2004b, *ApJ*, 612, L117